Seasonal and solar wind sector duration influences on the correlations of high latitude clouds with ionospheric potential.

Brian A. Tinsley[1], Limin Zhou[2], Liang Zhang[3], and Lin Wang[4]

[1]University of Texas at Dallas
[2]Key Laboratory of Geographic Information Science, Ministry of Education, East China Normal University, Shanghai, China
[3]Eastern Liaoning University
[4]East China Normal University

November 23, 2022

Abstract

Irradiances from long-lived stratus-type clouds at Alert (Canada), Summit (Greenland), and South Pole, previously measured, show correlations with the day-to-day input to the global atmospheric electric circuit from the solar wind, as well as with the inputs of low- and mid-latitude thunderstorms and shower clouds. We analyze the measured Alert cloud irradiances, and find differences in the responses to 2, 4, or more solar wind sectors per 27-day solar rotation. We find seasonal variations in the correlations, with sign reversal in the summer. The correlation coefficients that were found previously for all-year, all sector types show further increases for just winter months and in addition, for just 2-sector intervals. At high magnetic latitudes the ionospheric potential correlates strongly with the solar wind sector structure, and determines the flow of current density (Jz) to the Earth;s surface that passes through clouds and modifies space charge in them. Parameterizations of the potential distribution near the magnetic pole are used in the correlations. The daily average values depend mainly on the solar wind (interplanetary) magnetic field (IMF) By component, with lesser influence of the solar wind speed and IMF Bz. Mechanisms by which space charge in clouds can affect cloud microphysics and cloud opacity are described and are qualitatively consistent with the correlations, but need quantitative testing.

Hosted file

essoar.10504688.1.docx available at https://authorea.com/users/534742/articles/600952-seasonal-and-solar-wind-sector-duration-influences-on-the-correlations-of-high-latitude-clouds-with-ionospheric-potential

Seasonal and solar wind sector duration influences on the correlation of high latitude clouds with ionospheric potential

Brian A Tinsley[1], Limin Zhou[2], Lin Wang[2] and Liang Zhang[2]

[1]University of Texas at Dallas, Dallas, TX USA, [2]East China Normal University, Shanghai, China.

Abstract

Irradiances from long-lived stratus-type clouds at Alert (Canada), Summit (Greenland), and South Pole, previously measured, show correlations with the day-to-day input to the global atmospheric electric circuit from the solar wind, as well as with the inputs of low- and mid-latitude thunderstorms and shower clouds. We analyze the measured Alert cloud irradiances, and find differences in the responses to 2, 4, or more solar wind sectors per 27-day solar rotation. We find seasonal variations in the correlations, with sign reversal in the summer. The correlation coefficients that were found previously for all-year, all sector types show further increases for just winter months and in addition, for just 2-sector intervals. At high magnetic latitudes the ionospheric potential correlates strongly with the solar wind sector structure, and determines the flow of current density (J_Z) to the Earth's surface that passes through clouds and modifies space charge in them. Parameterizations of the potential distribution near the magnetic pole are used in the correlations. The daily average values depend mainly on the solar wind (interplanetary) magnetic field (IMF) B_Y component, with lesser influence of the solar wind speed and IMF B_Z. Mechanisms by which space charge in clouds can affect cloud microphysics and cloud opacity are described and are qualitatively consistent with the correlations, but need quantitative testing.

1. Introduction

1.1. The ionospheric potential - cloud microphysics - surface pressure hypothesis

The electrical structure of the solar wind is highly variable, on day-to-day and long timescales, as is the physical nature and occurrence frequency of cloud cover. Thus, it is very difficult to investigate reported small effects of the solar wind on cloud properties and atmospheric dynamics, especially in the context of the hypothesized connection through the global atmospheric electric circuit and through slow acting microphysical electrical processes with time scales of days; all very difficult to obtain reliable data on at cloud level. Also, the small signal/noise ratio on the day-to-day timescale makes analysis of subsets of the data even more difficult. Publications dealing with day-to-day correlations of atmospheric pressure at high latitudes with IMF changes include Wilcox et al., (1973); Mansurov et al., (1974); Page, (1989), Burns et al., (2007, 2008); Lam et al., (2013, 2014) and Zhou et al. (2018). The correlations of surface pressure at high latitudes extended over 1964-1974 (Page, 1989), and in 1995-2005 and 2006-2015 (Zhou et al. 2018). A positive correlation with IMF By or a proxy for it was found in annual data in all three time intervals in Antarctica at zero lag, and a negative correlation in annual data all three time intervals in the Arctic at zero lag. Opposite correlations in the Arctic and Antarctic are required for consistency with the solar wind effects on ionospheric potential in the proposed mechanism. Clouds at high latitudes (as the hypothesized amplifying intermediaries) have seasonal variations in ice and liquid phases and microphysical interactions. The variable nature of the solar wind sector structure and of the clouds is consistent with variability in correlation coefficients in subsets of the data, but has given rise to uncertainty as to the extent to which of biases of selection and processing of data have given unrealistically high values of statistical significance (p-values) for the correlations. Some of this uncertainty may be justified. However, irrespective of the actual p-values, the fact that all three decadal time interval in two widely separated regions gave consistent results for the simple, unselected cases of zero lag and annual data, makes a persuasive case for further investigations of correlations with the clouds themselves.

The hypothesis of Tinsley and Heelis (1993) was that these correlations might be due to the known solar wind – induced changes in ionospheric potential, which drives a flow of current down to the surface, affecting clouds on the way, and consequently affecting radiative coupling and surface pressure. Observations of correlations of cloud properties with solar wind magnetic field changes due to Kniveton et al., (2008), and Frederick and Tinsley, (2018) are consistent with this hypothesis. An amplitude for the temperature changes related to the cloud opacity changes was found to be of order 0.3K (Frederick et al., 2019) and peaking at about 0.7K (Lam et al., 2017). The surface pressure changes found were of order 1 hPa (Burns et al., 2007).

The day-to-day variations and both the meteorological data and the solar wind data have been observed for more than 50 years, and the B_Y input, with its reversals two or more times per month, offers a sufficiently long time series for correlations with meteorological parameters to separate out the effects of atmospheric electricity from those of the many other inputs into the weather and climate system.

The confidence one can place in the physical reality of the linkages can be gained by other considerations in addition to those of statistical significance. They include the Bayesian approach using additional independent data sets as noted above; by finding that the hypothesis can be extended to explain a wider range of phenomena than that for which it was formulated; and by showing the extent to which the hypothesis can be deduced from prior accepted knowledge. Thus extending the analysis to cover changes in ionospheric potential not caused by the solar wind, but by day-to-day variability in the electrical output of thunderstorms and shower clouds at low latitudes, provides additional source of confidence in the reality of the link between ionospheric potential and surface pressure. The current output is conducted to high latitudes in the lower ionospheric path of the global electric circuit. Consequently the day-to-day potential changes due to day-to-day changes in the atmospheric generators vary in the same way in both the Arctic and the Antarctic, instead of the opposite way for the changes due to the IMF B_y. These variations are superimposed on those due to IMF B_y, and constitute one of several sources of 'noise' for correlations only with B_y. Burns et al (2007) showed that measured day-to-day changes in vertical electric field (Ez) at Vostok for 1998-2001 (that combine the B_y input with the low latitude meteorological input) correlated positively with the station pressures with a lag of 2 - 3 days. To allow for persistence of the effect, a composite of the field values at lags between 1 and 4 days yielded a linear regression gradient with respect to Vostok surface pressure of 1 hPa per 10 V/m of electric field change, with 10% common covariance. This regression gradient is consistent with that from the IMF B_y effect alone. In addition, Burns et al (2008) used the same Vostok Ez data and the Weimer (1996) model values to remove the IMF B_y contribution from the measured daily Ez values, thus isolating the meteorological component. They found that not only for the combined 11 Antarctic sites examined were the regressions of surface pressure on Ez positive, but what is important is that for the 7 Arctic sites examined the regressions were also positive, consistent with theory, and in contrast to the negative correlations with IMF B_y in the Arctic. So these tests of extensions of the Tinsley-Heelis mechanism to the effects of the meteorological generators, separately from those of the solar wind generators, support the original hypothesis, as do the correlations with B_y over several additional independent sets of years beyond those that were used to generate the hypothesis.

Aspects of the support for clouds as an intermediate link are provided by Kniveton et al. (2008) which showed (their Fig. 4) cloud changes measure by satellites over Antarctica strongly and positively correlated with 1998-2001 day-to-day Ez measurements at Vostok. Further independent support comes from Frederick (2016, 2017), Frederick and Tinsley (2018), and Frederick et al. (2019). The first two papers showed correlations of cloud opacity at Summit, Greenland and the South (geographic) Pole with the daily magnetic Ap index, which is associated with ionospheric potential changes. The third showed positive changes in cloud opacity at the South Pole with the 1998-2001 measured values of Ez at Vostok, consistent with the Kniveton et al., (2008) satellite results. The fourth showed the expected negative correlations of cloud opacity at Alert Canada with B_y at 3-4 day lags, using all-year data. An indirect support for tropospheric clouds as one link in the chain was given by Lam et al., (2014, 2017) who showed that changes in geopotential height and in atmospheric temperature from Antarctic reanalysis data propagated upward from near the surface to about 10 km altitude, consistent with heating near cloud level.

None of the links in the hypothesized chain involve new physics; the quantitative adequacy has yet to be tested, but not the qualitative adequacy. So even without tests of statistical significance, these results provide very strong confidence for the validity of the ionospheric-potential - cloud - surface pressure linkage.

1.2. The global electric circuit at high magnetic latitudes.

The global atmospheric electric circuit is bounded by the earth’s surface and the highly conducting ionosphere, but the ionosphere is the lower boundary of the magnetosphere, and the ionosphere and magnetosphere do not entirely shield the middle and lower atmosphere from the highly conductive and electrically active solar wind. Inside the auroral ovals the near-vertical magnetic field lines connect to the solar wind and transmit electrical potentials generated by the solar wind Lorentz **V**x**B** electric fields to the Arctic and Antarctic ionospheres. Here **V** is the velocity of the Earth relative to the solar wind, directed towards the sun, and **B** is the interplanetary magnetic field (IMF), and the cross product gives an electric field perpendicular to both. The east-west, or B_y, component of the IMF gives an electric field which is positive from south to north. The ionospheric potential up to 15° from the south geomagnetic pole is increased, depending on B_y, by 20 kV or so on average, while depressed near the north geomagnetic pole by about the same amount (e.g., Tinsley and Heelis, 1993, Lam et al., 2013). There are also potentials on the dawn and dusk side of the auroral ovals generated by solar-wind-induced field-aligned magnetospheric currents. The solar wind magnetic field, and thus its B_Y component (IMF B_Y) and the ionospheric potential inputs, reverse frequently, at times twice or four or more times per 27-day solar rotation, creating the sector structure as observed by Ness and Wilcox (1965), with corresponding reversals of the B_Y input to the high magnetic latitude ionospheres. Daily average values of B_Y are available at the NASA/GSFC web site (NASA, 2018). Based on the B_Y variations, the time series can be divided into intervals which we treat as 2-sector, 4-sector, or variable (irregular or more than 4) sector intervals. Figure 1 shows four years of variations of B_Y as well as of B_Z (the north-south IMF component) and the solar wind speed, from the NASA/GSFC web site, and examples of our characterizations. The solar wind data are complete, except for a few days in late 2004, for which we used interpolations.

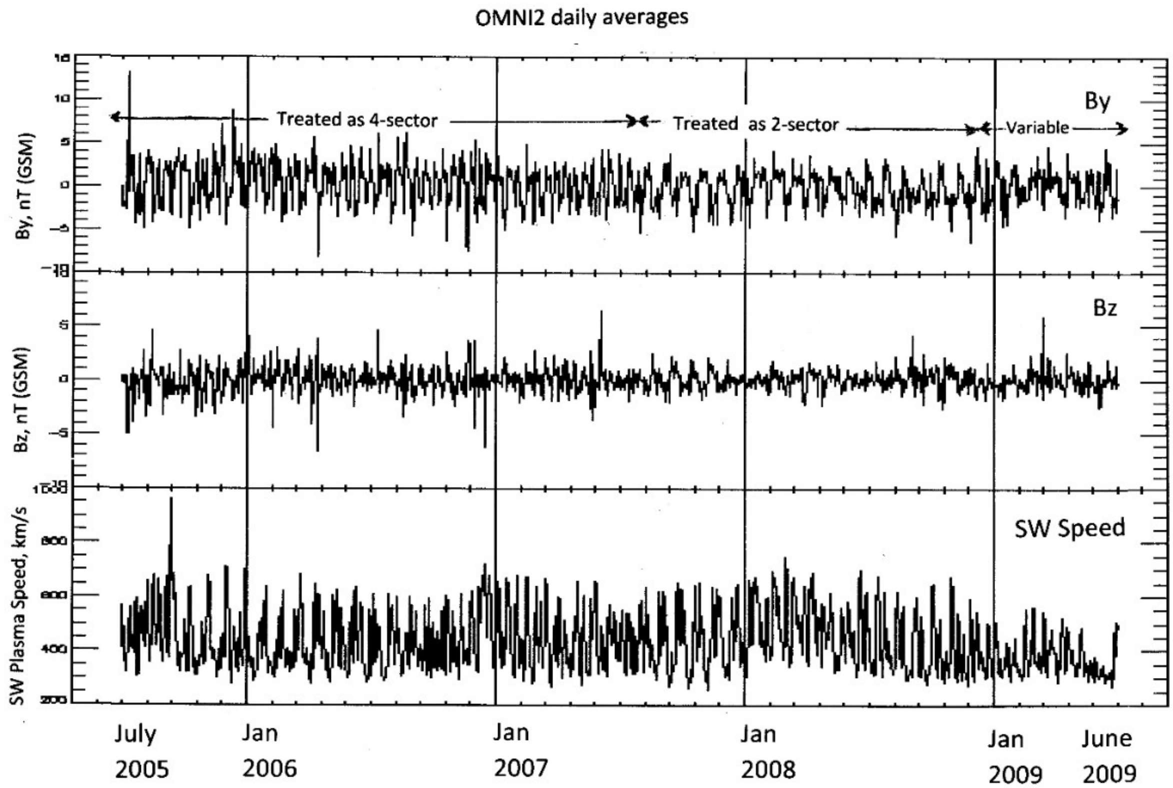

Figure 1. Time series of IMF B_Y (top panel), IMF B_Z (middle panel) and solar wind speed (lower panel) July 2005 to June 2009, from NASA (2018). Intervals of sector structure are designated 2-sector, 4-sector or variable (irregular or more than 4 sectors). The 2-sector structure begins in July 2007.

The solar wind-induced polar ionospheric potential changes are superimposed on an otherwise nearly globally uniform but time-varying ionospheric potential, generated by thunderstorms and highly electrified convective clouds at low latitudes (e.g. Hays and Roble, 1979, Roble and Hays, 1979). These meteorological generators send a total of about 1000 Amperes to the ionosphere and charge it electrically to a potential of about 250 kV. All over the globe this potential difference between the ionosphere and the surface drives a downward current density of order a few pA/m^2, and as if flows through clouds it alters the amount of electric charge, due to ionization by galactic cosmic rays, that would otherwise be on droplets and aerosol particles. The current density, at a given location and in the absence of changes in atmospheric aerosol and in the cosmic ray flux, is proportional to the overhead ionospheric potential (Tinsley, 2008). Measured vertical electric field values at ground level, which are proportional to current density, made close to the southern magnetic pole at Vostok, show the expected changes as B_Y changes at sector boundaries (Burns et al., 2006, Figs. 2 and 3).

Figure 2 shows diagrams of northern hemisphere dawn-dusk section of the global circuit. The top panel is from Markson (1983), showing the low latitude convective cloud generators and the high dawn and low dusk potentials near the auroral zone that are due to magnetospheric currents driven by IMF B_Z. The lower panel is from Tinsley and Heelis (1993) showing the reduction of ionospheric potential within the northern auroral zone due to positive IMF B_Y, and the increase there due to negative B_Y. We use the term ‘polar cap’ as equivalent to this area affected by B_Y, for which more details are given in Appendix B. The average of the potential distribution over the area of the polar cap, and over time, varies most strongly with IMF B_Y, as determined by the sector structure, except during magnetic storms.

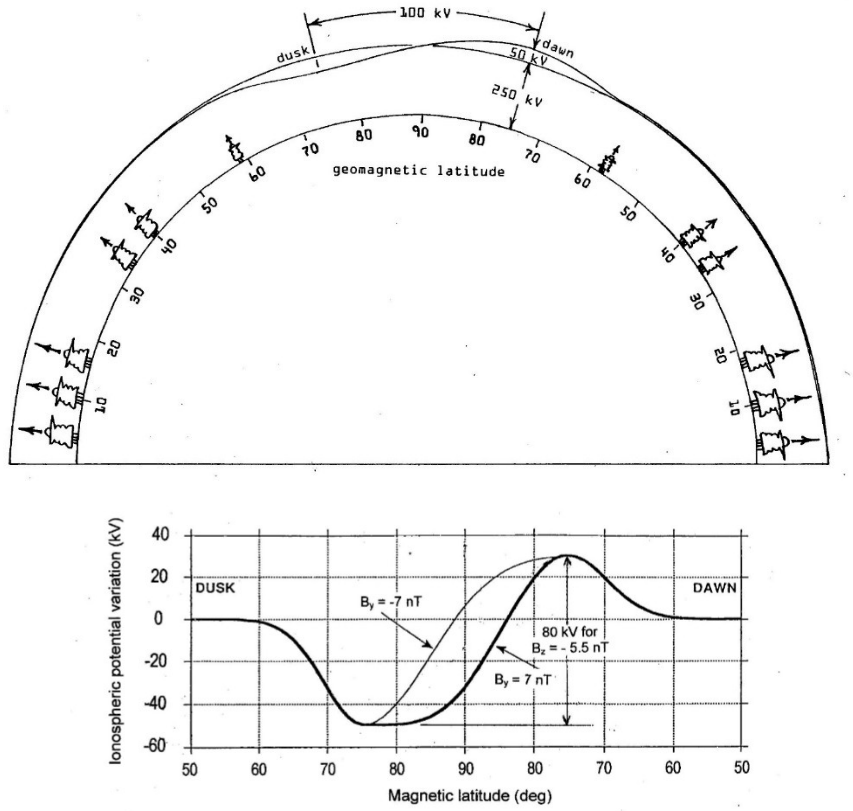

Figure 2. Diagrams of East-West sections through the northern hemisphere of the global electric circuit, top: from Markson, (1983) showing the dawn and dusk ionospheric potential changes induced by IMF B_Z, and bottom; from Tinsley and Heelis, (1993) the potential changes induced by IMF B_Y.

There is theory and evidence, reviewed by Lam and Tinsley, (2016) that the changes in the downward current density (J_Z) in the global circuit have small but significant effects on the electric charges on, and the collision rates of, droplets and aerosol particles. These can affect microphysical processes in clouds, and cloud development, but such effects are difficult to distinguish from all the other inputs that contribute to variability in clouds The polar cap B_Y-related potential variations are only 20% or so of the total ionospheric potential, and cover only about 4% of the globe, but the stratus-type clouds in polar areas persist for days, allowing time for small changes in the microphysics that affect condensation nuclei concentrations and ice production to accumulate. The clouds are often of optical thickness less than unity, and so that they are particularly sensitive to changes in their microphysics that can affect their optical thickness and their radiative coupling to the atmosphere (Mauritsen et al., 2011).

Alert, Canada is about 3° from the north geomagnetic pole, and continuous observations of downwelling and upwelling infrared irradiance have been made there since 2004, and are available at the NOAA web site (NOAA 2018). It was shown by Frederick et al. (2019) that the daily average irradiances 2004-2015 showed statistically significant correlations with the IMF B_Y component, with a lag of 3 or 4 days. The observed amplitude was equivalent to cloud and surface temperature changes of about 0.3° C. This lag of several days raises the question of how the surface pressure variations are related to the cloud opacity variations. Such relationships between cloud opacity and cloud radiative forcing are expected (Ramanathan et al., 1995), but the clouds and the atmosphere have their own internal dynamics and seasonal variations, which can affect phasing of the coupling of periodic variations.

In this paper we examine how the phase relationships of the irradiance to the solar wind sector structure vary through the seasons, as a clue to their relationships to each other. We examine how the amplitude of the responses change with the number of sectors per solar rotation. We also discuss hypothetical cloud microphysical mechanisms. Such mechanisms include electric charge effects on scavenging of aerosol particles by droplets, and so may also be sensitive to aerosol concentrations changes, changes in atmospheric circulation, and solar cycle changes in the solar wind; however we postpone for future work such considerations.

2. Observations at Alert of irradiance variations

The daily average infrared irradiances at Alert have an annual variation with a maximum in summer, as illustrated by Frederick et al. (2019). For use in correlations and for in superposed epoch analyses with respect to the solar wind input, the daily values of the downwelling and upwelling infrared irradiances were smoothed with a running mean, covering 13 days before and after the central day, but excluding that day, and the differences of the observed values from the running means evaluated. Figure 3 is of a time series of the correlations between the differences for the upwelling irradiances (U_IR) and the differences for the downwelling irradiances (D_IR) in a running 27-day window. The time series runs from 2004 to 2015. The correlation coefficient of D_IR and U_IR is around 0.8 in the winter, but decreases and becomes negative, reaching about - 0.5 in July-August of each year. This effect can be understood in terms of the optical thickness of the overhead stratus-type clouds increasing and decreasing. In the absence of sunlight in winter, thickening of clouds, whether or not due to atmospheric electricity, reduces the escape of radiation to space, and warms both the clouds and the surface. In sunlight, however, thickening clouds cool the surface by reducing the sunlight reaching it, more than their increased thickness radiates more heat downwards. In Fig. 3 other effects may be due to melting snow cover and mid-summer convection. Data for June-July 2007 and some smaller intervals in 2013-2014 is not available.

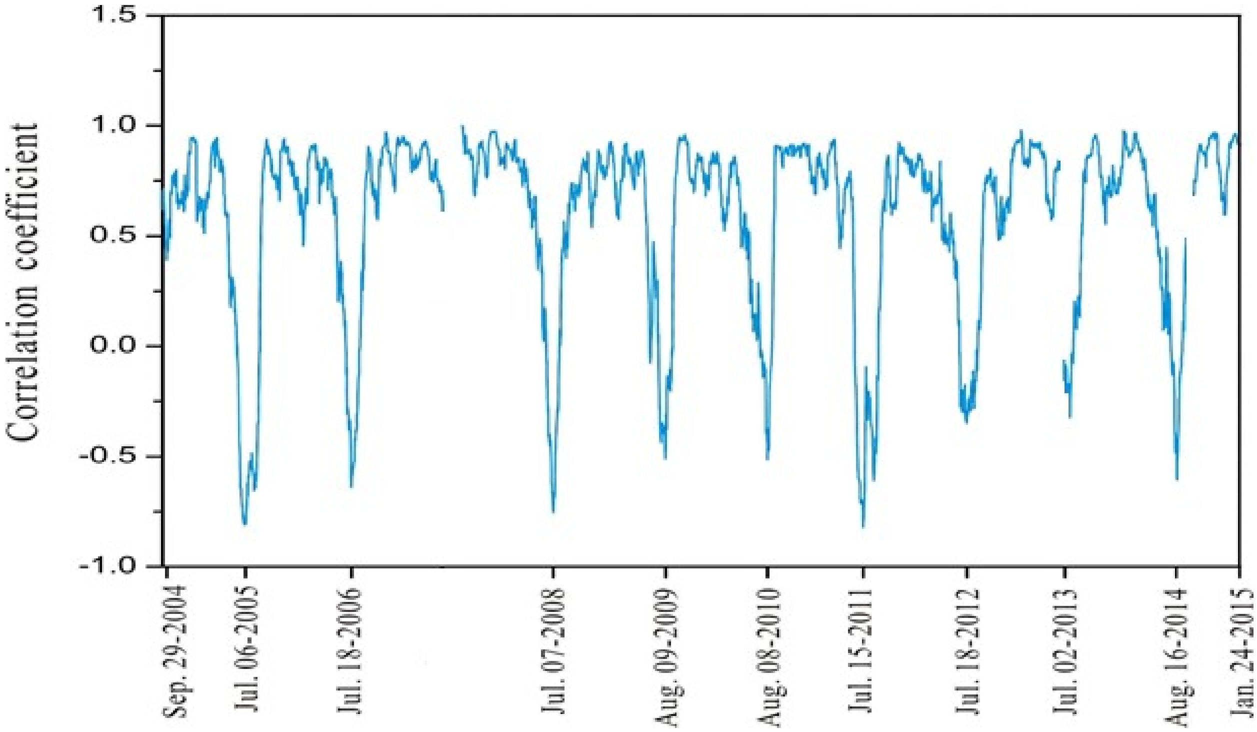

Figure 3. Correlation in a running 27-day interval between the daily mean downwelling infrared irradiance (D_IR) and the upwelling irradiance (U_IR) measured at Alert, Canada 2004-2015. Data for June-July 2007 and small intervals in 2013-2014 are missing.

The sector structure of the solar wind can vary from 2-sector to 4 sector to multiple and irregular sector structures over intervals of a few months to a few years, as in Fig. 1. Previous work has shown that a duration of at least 4-days for a given polarity of B_Y is required in superposed epoch analyses with meteorological parameters to obtain significant correlations. According to the theory reviewed by Lam and Tinsley (2016) this is consistent with the time constants for the cloud microphysical processes to take effect, and we would expect differences in the correlations found with intervals of 2-sector structures as compared to those with 4-sector structures or with intervals of multiple or irregular sectors. Our exploratory analyses (not shown), found small and variable correlation coefficients for the latter. A table of intervals of these sector types, designated by inspection of plots such as in Fig. 1, from 1993 to 2018, is given in Appendix A.

Because a positive excursion of IMF B_Y produces a negative excursion of ionospheric potential in the northern polar cap and to a positive excursion in the southern polar cap, a general treatment for correlations with sector structure in both hemispheres is preferably made in parameters representing ionospheric potential. In Appendix B we show the results of fitting parameters to the model by Weimer (1996) that is based on satellite measurements of potential as a function of solar wind parameters. This parameterization allows us to take into account the small effects of the solar wind speed, Vsw, and the IMF B_Z component, as well as the major effect of IMF B_Y on both the potentials for the north and south magnetic poles (VpN and VpS respectively). The solar wind parameters are available on an hourly basis but we use daily average values for calculating the daily average VpN values. Although there is are polynomial terms in Vsw in the fit to VpN, the hour-to hour changes in Vsw are relatively small, and from tests we made there are negligible differences for the correlations in using daily average solar wind inputs for VpN, rather than making daily averages of hourly values of VpN.

2.1. Correlations of Alert irradiance variations with ionospheric potential.

Figure 4 shows lagged correlations of D_IR and U_IR with negative IMF B_y and VpN, for all months and for all sector types. This is an extension of an inverted version of the Figure 5 of Frederick et al (2019), and is a plot of correlation coefficient rather than regression coefficient. Frederick et al. (2019) showed that the response to B_Y is significant at about the 95% level. The correlation coefficients in Fig.4 exhibit a strong solar rotation 27-day repetition, implicit in the sector structure. The 2004-2015 period covers 144 solar rotations. Positive lags in this and following figures are for solar wind variations leading the irradiance variations.

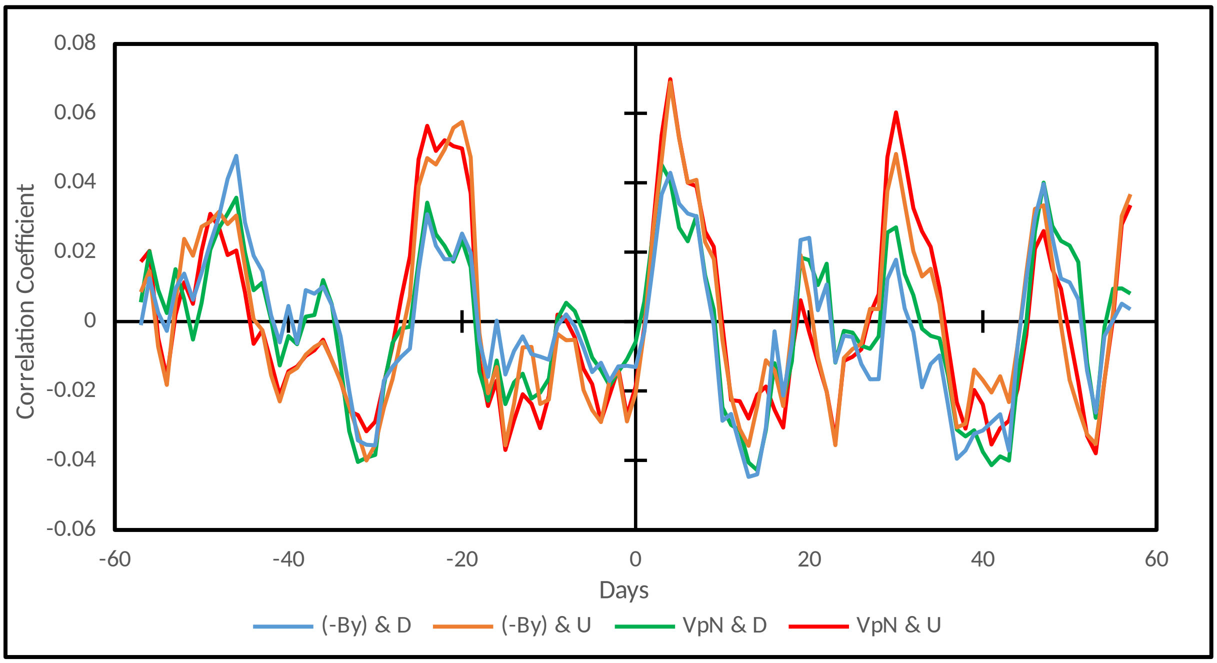

Figure 4. Lagged correlations for all seasons and all sector types of D_IR and U_IR with ($-B_y$), blue and orange curves respectively; and with VpN, green and red curves respectively, 2004-2015.

The results of Fig. 3 which show the correlation coefficient between D_IR and U_IR in the summer months departing from, and reversing in mid-summer from the values for the rest of the year, show that in the summer months the irradiances behave differently from the rest of the year, and should not be included with them in the correlation analyses. October-April months should be mostly clear of these effects, and Figure 5 shows the same analysis as Fig. 4, but restricted to October through April intervals. The correlation coefficients now range up to 0.1, and there is less difference between the U_IR and D_IR curves.

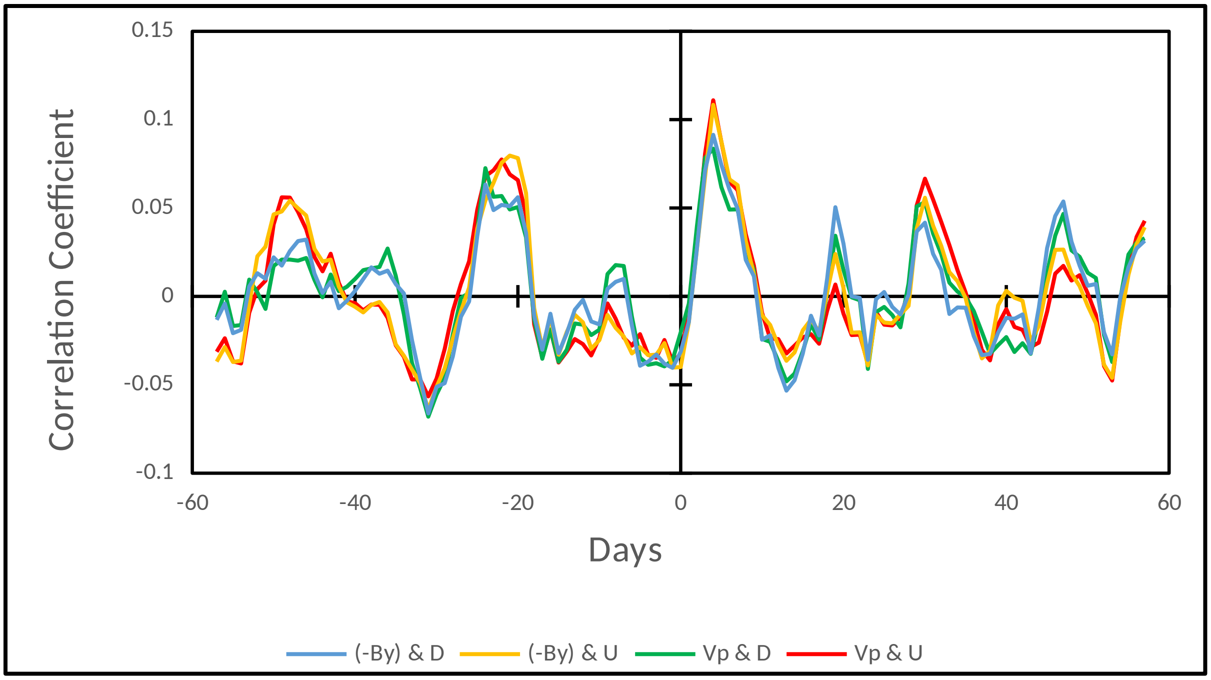

Figure 5. Lagged correlations for each October through April and all sector types of D_IR and U_IR with (-B_y), blue and orange curves respectively; and with VpN, green and red curves respectively, 2004-2015.

Figure 6 shows correlations of the irradiances with VpN for combined 2 and 4-sector intervals only, for October through April intervals of D_IR (blue) and U_IR (red); also for each June-August with D_IR (grey) and U_IR (yellow). For October-April intervals, the results are similar to those of Figure 5 which included variable and irregular intervals of solar wind structure. For June-August the results for U_IR and D_IR are of out of phase with those for October-April, and those for D_IR are opposite to those for U_IR. This is expected from the results of Fig. 3, and justifies the restriction of further analyses to October-April months.

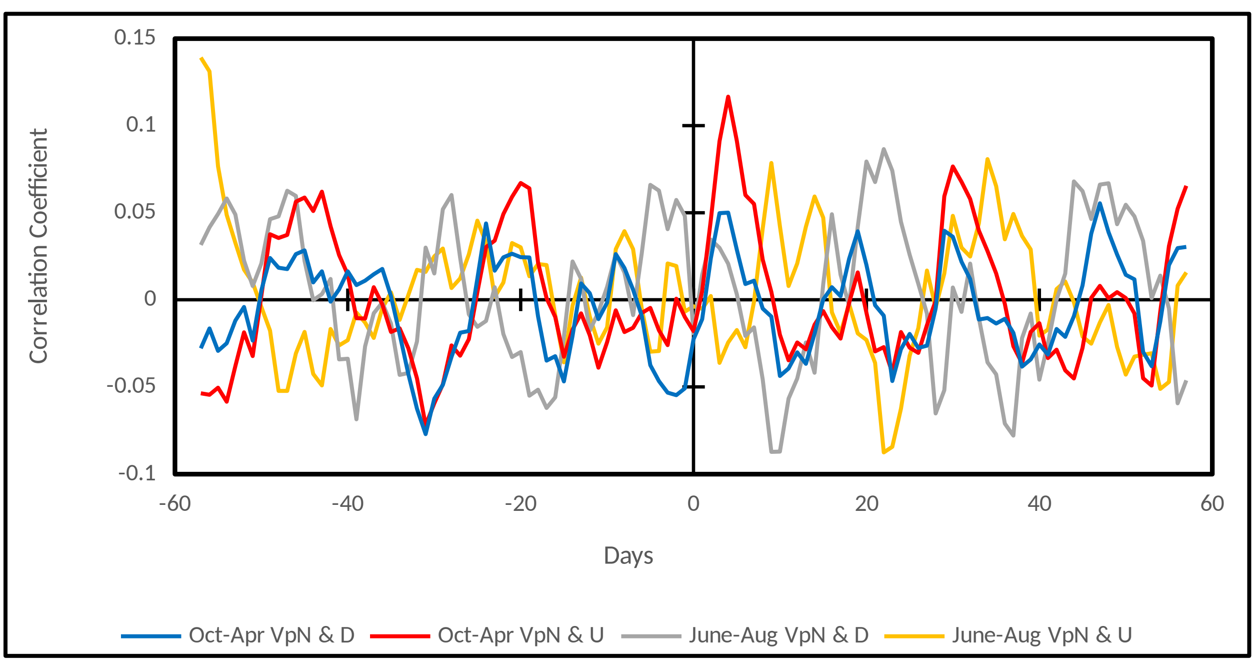

Figure 6. Lagged correlations with VpN for each October through April of D_IR (blue) and U_IR (red); also for each June-August with D_IR (grey) and U_IR (yellow); for combined 2 & 4 sector solar wind intervals, 2004-2015.

Figure 7 shows lagged correlations of only 2-sector U_IR values with VpN for all October-April months in which they occurred during 2007-2008 (orange) and during 2010-2015 (blue) with the overall correlation in black. They are of larger amplitude, reaching a correlation coefficient of 0.2, than the correlations for combined 2 & 4 sector segments, partly because successive 4-sector segments occur at a variable spacing within repeating 27-day periods structures. In view of the lag time for the responses, it may also be because each 2-sector variation lasts twice as long as a 4-sector variations, this allows a greater response to develop. The correlations are a little stronger for the solar minimum period 2007-2008.

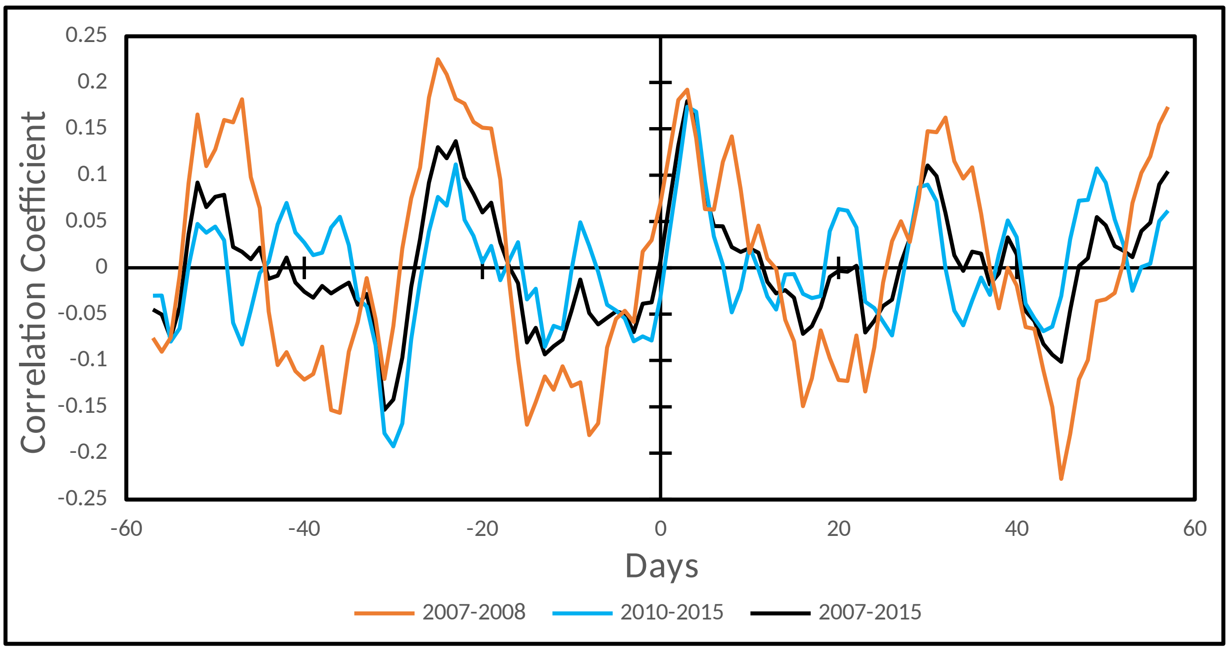

Figure 7. Lagged correlations of 2-sector U_IR values with VpN for October-April intervals: Oct 1 2007 to Nov 17 2008 (orange); Jan 11 2010 to Feb 22 2015 (blue): Overall correlation, (black).

2.2. Correlations for irradiances across sector boundary types

The previous analyses of correlations do not show possible differences in the cloud response to increases in ionospheric potential as opposed to decreases in ionospheric potential. So the data were stratified into 14-day portions, centered on either a negative to positive Sector Boundary Crossing (SBC), or a positive to negative SBC. Since the work of Wilcox et al., (1973) it has been recognized that to see correlations of atmospheric data with solar wind sector structure, an interval of at least 4 days of one sign of magnetic field before the boundary, and at least 4 days of the opposite sign afterwards is needed. The obvious physical justification was that the atmosphere took some days to respond fully to the solar wind input. Because Frederick et al. (2019) had found a lag of 3-4 days when correlating irradiance with B_Y, and we wanted to minimize interference with the previous and following SBCs, we made averages of VpN of the 7 days before the SBC, and averages of the 7 days after. We used the average from day -7 to day -1 as a substitute for the actual VpN for days -14 to -8. We used the average from day +1 to day +7 as a substitute for days 8 to 14 in the correlations. Then the lagged correlation could be made over the 7 days before or after zero lag, without decreasing the number of data points for the larger positive or negative lags. The shortened winter period of October-March is used to focus more on the cold season and minimal sunlight. Instead of selecting SBCs by the change in sign of B_Y extending from 4 days before to 4 days after a SBC, we select SBCs on the basis of them having the average VpN of the four days before the SBC, minus the average for the four days afterwards, being a change of at least 10 kV. In addition, in order to minimize noise and overlapping sectors, we required that there be no days with values of VpN in the five days before or after the SBC that differed from the average of the seven days in the corresponding period before or after by more than the difference of the two seven-day averages.

Figure 8 shows the result for positive to negative SBCs, for all selected sectors, for D_IR (grey) and U_IR (yellow), and for just 2-sectors for D_IR (orange) and U_IR (green). There were 52 SBCs all-sector and of these 19 two-sector SBCs satisfying the above selection criteria in the data for 2004-2015.

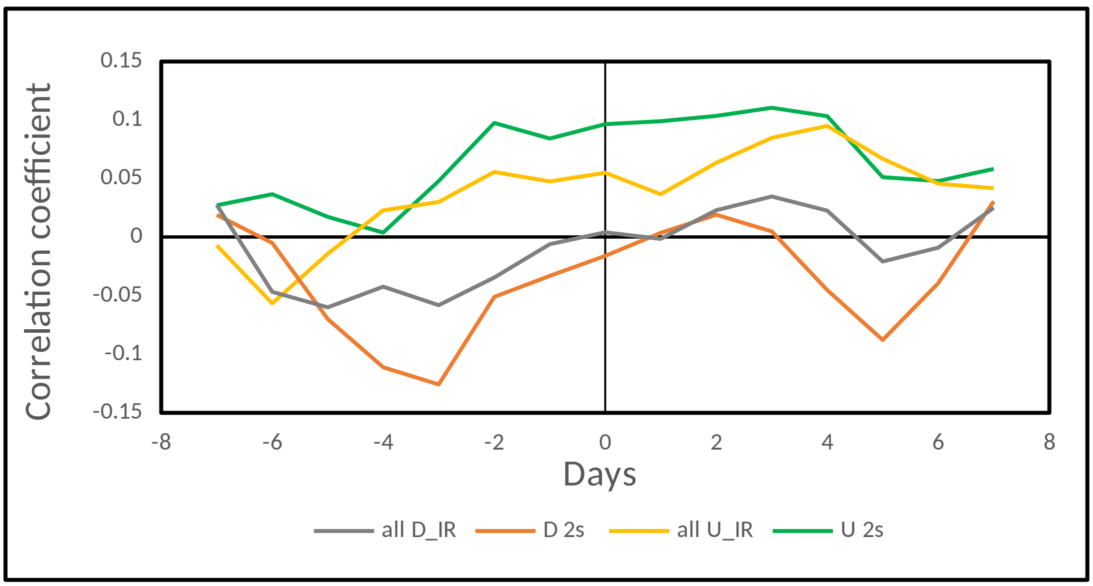

Figure 8. Lagged correlation with VpN for isolated -7d to +7d portions of + to - SBCs of Alert irradiance data, 2004-2015. For October-March intervals for all sectors, D_IR (grey) and U_IR (yellow); and for just 2-sectors, D_IR (orange) and U_IR (green). There were 52 SBCs all-sector and 19 two-sector SBCs in this analysis.

Figure 9 shows the corresponding result for negative to positive SBCs, for all sectors for D_IR (grey) and U_IR (yellow), and for just 2-sectors for D_IR (orange) and U_IR (green). There were 47 all-sector and of these 14 two-sector SBCs satisfying the selection criteria.

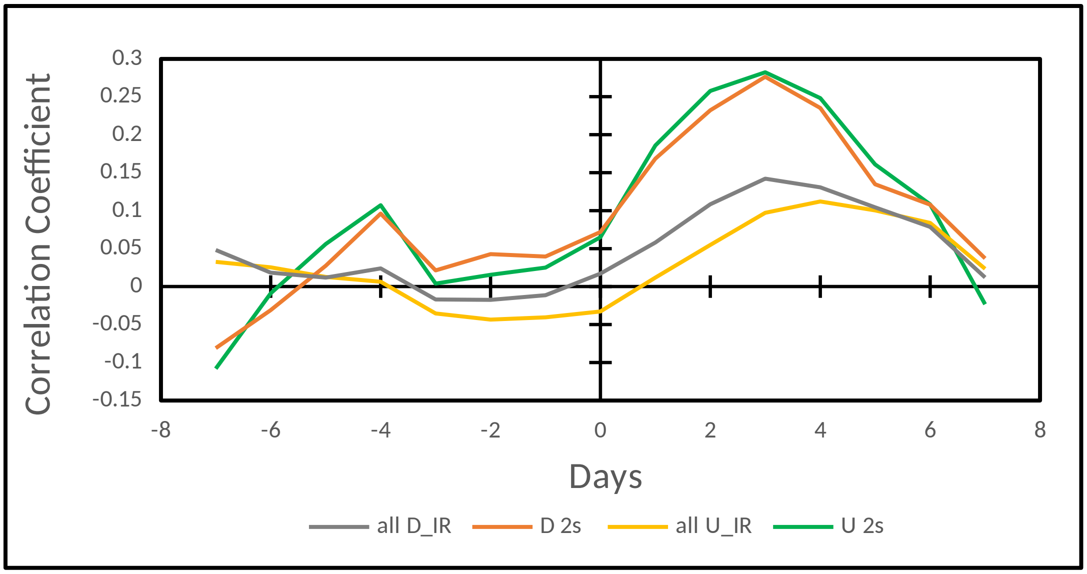

Figure 9. Lagged correlation with VpN for isolated -7d to +7d portions of – to + sectors of Alert irradiance data, 2004-2015. For October-March intervals for all sectors, D_IR (grey) and U_IR (yellow); and for just 2-sectors, D_IR (orange) and U_IR (green). There were 47 SBC all-sector and of them 14 two-sector SBCs in this analysis.

The lag in peak positive correlation and in the drop in correlation afterwards is about 2 to 4 days in Fig 8, in comparison with lags of about 3-4 days lag in Fig 9, but this difference, and the differences in the shapes of the curves, could be an effect of noise, i.e., unrelated day to day variations, in the data. Comparing changes in correlation coefficient for SBCs in 2-sector intervals with the all-sector correlations and with the correlations of Fig 8 and the comparison of Figs 5 and 7, we see again larger amplitude of changes, notably from days 3 to 5, for the 2-sector crossings than for the all-sector crossings. The fluctuations prior to day −4 may include the delayed responses to the previous SBC.

We consider the important results of Section 2.2 to be (1) the correlations peaking with positive lags of 2 - 4 days in spite of the small data samples necessitated by separating the +/- and -/+ transitions and separating the 2-sector structures from the all-sector structures; and (2) no evidence for differences in the lags for -/+ SBCs as compared to +/- SBCs in these data samples, (3) the larger (lagged) changes in correlation coefficients across the SBCs for the 2-sector structures as compared to those for the all-sector SBCs, as seen in comparing Figs. 5 and 7.

2.3. Superposed epoch irradiance analysis

In addition to making separate correlation analyses for – to + and + to – SBCs, we can make separate superposed epoch analyses of irradiance across the SBCs. The number of data points going into the averages for each day before or after the boundary is further reduced from the set of all the data points generating each value on the lagged correlation analyses of Figs. 4-7, and so the noise levels are correspondingly increased. Nevertheless, we show in the following figures superposed epoch analyses for the available data. To clarify the trends the results in the following two figures have been smoothed with a (1:2:1)/4 running mean.

Figure 10 shows superposed epochs of irradiances for Alert for + to – sector boundary crossings. There were 52 all-sector and of them 19 two-sector crossings satisfying the selection criteria. The units of irradiance are W/m^2 and standard errors of the mean for the unsmoothed data 3.8 W/m^2 for all sector D_IR; 2.7 W/m^2 for all sector U_IR; 5.7 W/m^2 for 2s D_IR; 2.3 W/m^2 for 2s U_IR. These were calculated from the standard deviation of the values for each individual epoch at each lag. For the ionospheric potential change, 6 units of VpN/3 correspond to 18 kV. At a mean cloud temperature of 256K, 5 W/m^2 corresponds to a change in temperature of 1.3 K.

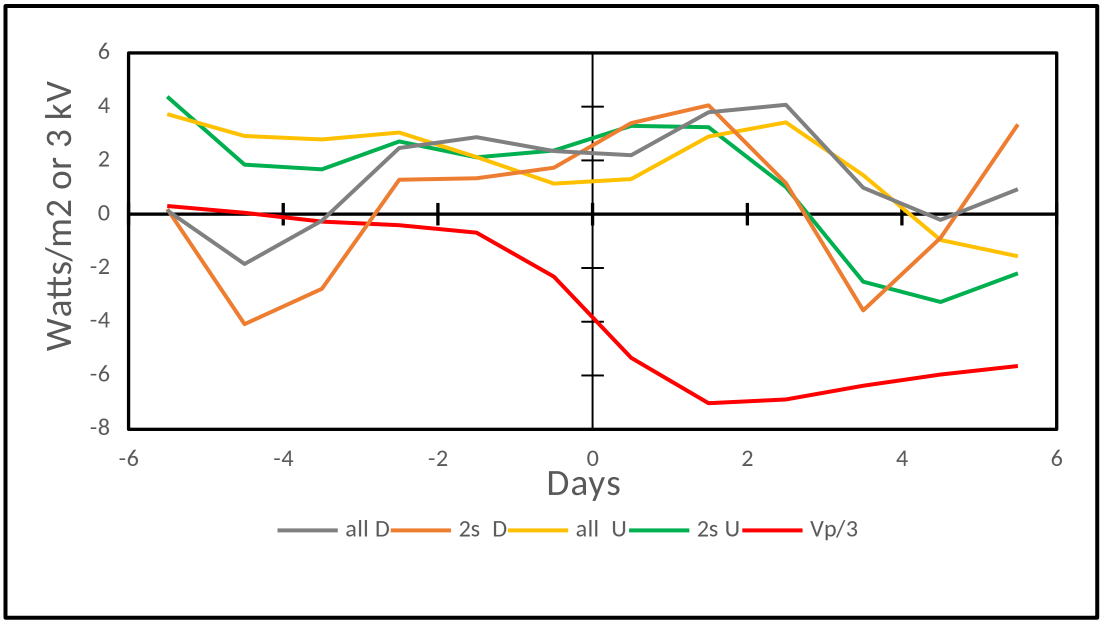

Figure 10. Smoothed superposed epoch analyses of changes in Alert irradiances across + to - sector boundaries, for all-sector D_IR (grey) and U_IR (yellow) and 2 sector D_IR (orange) and U_IR (green). The irradiance changes can be compared to changes in VpN/3 (red). Data for each October through March, 2004-2014. The units of irradiance are W/m^2. Six units of VpN/3 correspond to 18 kV of the ionospheric potential change. There were 52 all-sector SBCs and of them 19 two-sector SBCs in this analysis.

Figure 11 shows the corresponding superposed epochs of irradiances for Alert for – to + sector boundary crossings. There were 47 all-sector and of them 14 two-sector SBCs in 2004-2015 satisfying the selection criteria of Section 2.2. The units are the same as for Fig. 10. The results of both Figs 10 and 11 are consistent with the lags of 2 to 4 days for the response of the irradiances to the changes in overhead ionospheric potential and the correlation analyses of Figs 4-9. The standard errors of the mean for the unsmoothed data average 3.8 W/m^2 for all-sector D_IR; 2.8 W/m^2 for all-sector U_IR; 7.0 W/m^2 for 2s D_IR; 5.3 W/m^2 for 2s U_IR. These were calculated from the standard deviation of the unsmoothed values for each individual epoch at each lag.

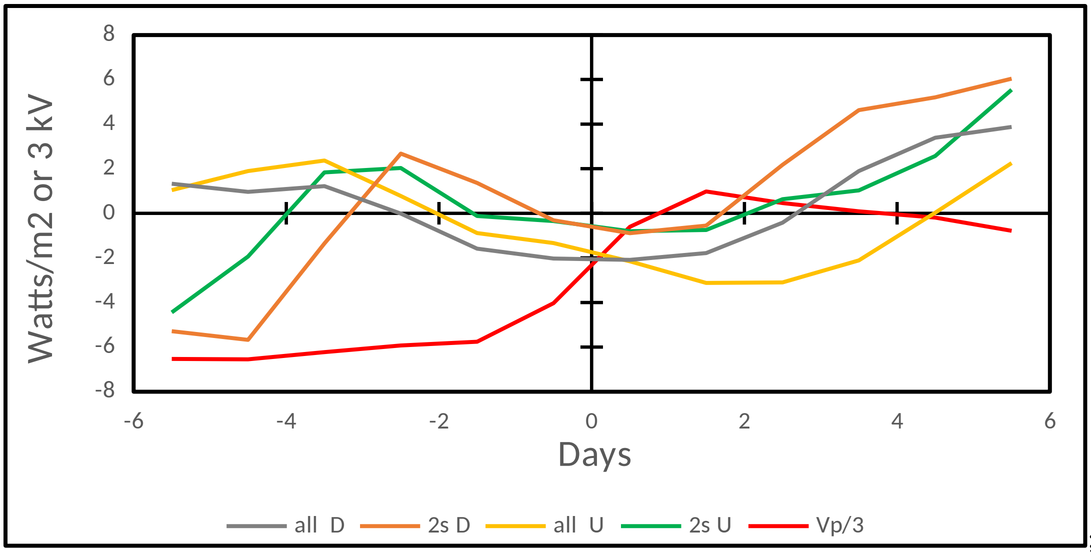

;

Figure 11. Smoothed superposed epoch analyses of changes in Alert irradiance and VpN across – to + sector boundaries, for all-sector D_IR (grey) and U_IR (yellow) and 2-sector D_IR (orange) and U_IR (green). The irradiance changes can be compared to VpN/3 (red). Data for October - March, 2004-2015. The units of irradiance are W/m^2. Six units of VpN/3 correspond to 18 kV of the ionospheric potential change. There were 47 all-sector SBCs and of them 14 two-sector SBCs in this analysis.

Comparing the result for + to – boundary crossings (Fig. 10) with those for – to + crossings (Fig. 11), we consider the important results not to be in the statistical significance of the results, but in the reversal of the trend across the sector boundaries, and especially for the lagged response in days 2 to 5.

3. Discussion of hypothesized mechanism

An obvious inference is that our results for changes in cloud irradiances that correlate with IMF B_y and overhead ionospheric potential, and for the upwelling irradiance that correspond to changes in surface temperatures at the same locations, are the cause of the changes in surface pressure (Burns et al., 2008; Lam et al. 2013, 2014) which also correlate with B_y at high magnetic latitudes. However, if so, there is inter-annual variability of the pressure changes compared to the ionospheric potential and irradiance changes, which is not yet understood. We made the correlations in terms of the calculated ionospheric potential VpN instead of B_Y because the ionospheric potential depends on B_Z and the solar wind speed as well as on B_Y. The use of ionospheric potential rather than B_Y points to the importance of this component of the global electric circuit as a linkage between the solar wind and terrestrial parameters.

Another inference is that our results for the correlations of cloud and surface irradiances with ionospheric potential are caused by the same cloud processes the are involved in the correlations of temperature and surface pressure in the Antarctic with internal (thunderstorm and shower cloud) global circuit sources of ionospheric potential changes (Burns et al., 2008: Frederick and Tinsley, 2018). Ionospheric potential changes from either source entail changes in electric currents flowing from the ionosphere to the surface through clouds.

As the ionosphere-Earth current density flows through a cloud, here is an accumulation of space charge in the gradients of conductivity at the cloud boundaries (Zhou and Tinsley, 2007, 2012; Mareev, 2008; Nicoll, 2012; Rycroft et al., 2012; Nicoll and Harrison, 2016). Space charge is an excess of charge of one sign, which is required by Poisson's equation to balance the gradient of electric field due to the current flowing through the gradient of conductivity. The conductivity gradient is caused by increasing attachment and recombination of air ions on the surfaces of droplets going into the cloud. While Pruppacher and Klett (1997, pp 796-7) showed that to the first order the collision rates of aerosol particles with each other was unchanged if there were equal numbers of positive and negative charged particles, this is not the case where there is an excess of charges of one sign. In this case the excess of repulsive encounters reduces the collision rate, and similarly for collisions between particles and small droplets. We call this reduction in collision rate and therefore in scavenging rate due to Coulomb repulsion, electro-anti-scavenging. The opposite process, electro-scavenging, due to the attractive electrical image force, is the increase in collision and scavenging rates, and is important for larger particles and droplets.

The flow chart in Fig. 12 illustrates established and hypothesized links in two possible chains of linkages from the solar wind through atmospheric electricity, electro-scavenging and/or electro-anti-scavenging, to tropospheric clouds, radiative coupling and/or latent heat release, to atmospheric dynamics. Discussion of various aspects of these and other linkages has been made in previous review papers (Tinsley, 2008; Rycroft et al., 2012; Lam and Tinsley, 2016). Recent papers include those on correlations of surface pressure with B_Y (Zhou et al., 2018) and correlations of irradiance with B_Y (Frederick et al., 2019). Correlations of meteorological parameters with Vsw and B_Z have been observed by Boberg and Lundstedt (2003) on the seasonal and decadal timescales. It is possible that these correlations would also be found by using parameters such as VpN and VpS instead of Vsw and B_Z only.

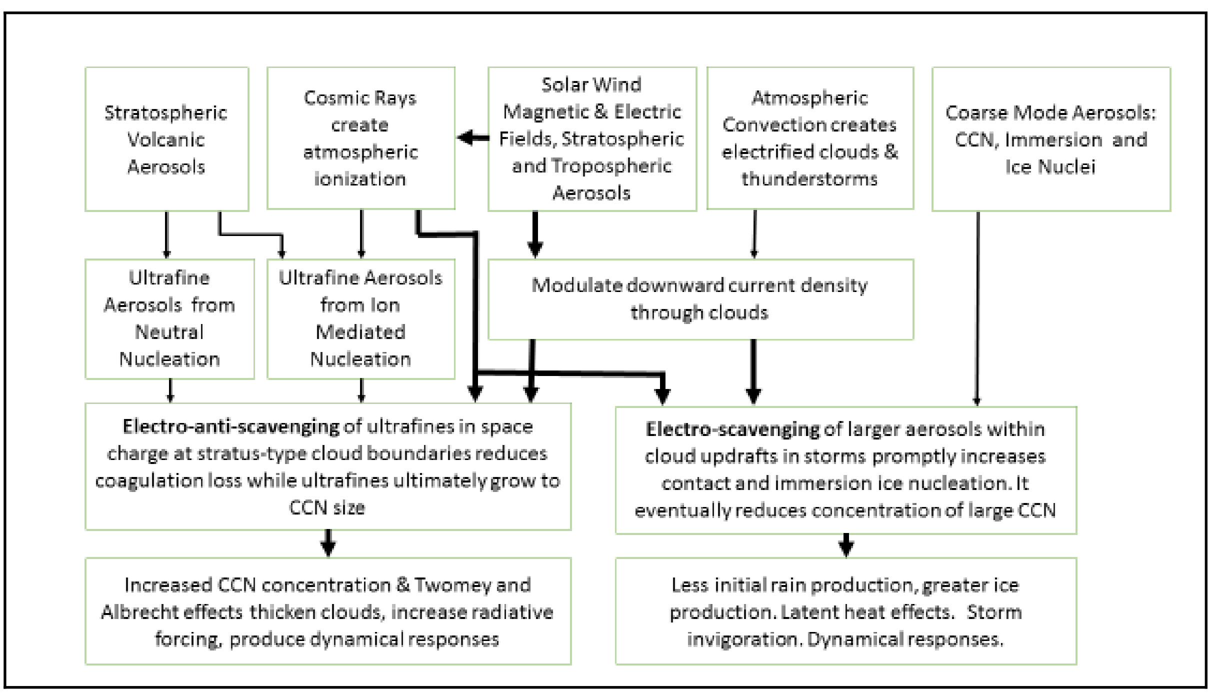

Figure 12. Flow chart of inputs and links influencing atmospheric electric interactions with clouds. Links involving deposition of electric charge on droplets and aerosol particles, influencing the microphysical electro-scavenging and electro-anti-scavenging processes in clouds, are shown in heavier lines.

The cloud microphysical theory underlying the concepts of electroscavenging and electro-anti-scavenging is well known, based on work reviewed, especially in Chapter 18, in the book by Pruppacher and Klett (1997) and the extensive references therein. Many of those papers, and subsequent ones, e.g., Khain et al., (2004), focus on charged droplet-droplet collisions. The work of Lu and Shaw (2015) deals with charged droplets in turbulent clouds; that of Di Renzo et al., (2019) deals with the effect of charged particles combined with electric fields in turbulent conditions near conducting walls. The effect of electro-scavenging on collisions involving ice crystals has been reviewed by Wang (2002). For significant effects on droplet-droplet collisions or droplet-ice crystal or crystal-crystal collisions thousands of elementary charges are required (Lu and Shaw, 2015) as in thunderstorm clouds, but the charges required on droplets in droplet-aerosol particle collisions in thin stratus-type clouds at high latitudes for significant microphysical changes are very much smaller.

Electro-scavenging of contact ice nuclei and immersion ice nuclei would increase ice nucleation and increase precipitation and reduce cloud opacity. The consequent reduced infrared irradiance would be contrary to observations. We are left with electro-anti-scavenging of aerosol particles in space charge as the only candidate we know about for a microphysical mechanism that would increase droplet or ice crystal concentration (while reducing their average size) and thus causing increases in infrared opacity by the Twomey (1977) effect. We hope that if there are viable alternative mechanisms to electro-anti-scavenging that can account for the correlations this paper will stimulate publication of them.

Since the review by Pruppacher and Klett (1997) electrical effects on electro-scavenging and electro-anti-scavenging of aerosol particles by droplets has been treated by Tinsley et al., (2001); Tripathi et al., (2006), and with comprehensive numerical modelling in a series of papers by Zhang and Tinsley (2017, 2018), and Zhang et al., (2018, 2019). Electro-scavenging involves the electric image force, and is more applicable to larger droplets and particles, with larger charges. The electro-anti-scavenging process, involving the electric Coulomb force, is the one applicable where space charge is present, and is effective for small and ultrafine aerosol particles and smaller droplets with small charges, where diffusive transport dominates over fall speed, as in the case of the long-lived stratus-type clouds observed in the high latitudes.

The lifetime for removal of aerosol particles by Brownian collisions with droplets in a typical cloud is about 40 minutes (Pruppacher and Klett, 1997, p. 723). An excess of charge of one sign can prolong this lifetime by increasing the proportion of repulsive encounters, so that over the course of days there is a significant reduction in scavenging. Thus there is an increase in the concentrations of interstitial and evaporation nuclei, and especially in those of the abundant ultrafine aerosol particles (Humphries et al., 2016) in high latitude upper tropospheric regions, that can mix into clouds and grow to condensation nuclei size in volatiles contained in the clouds. With increased concentrations of condensation and ice nuclei, during the continual in-cloud microphysical processing during vertical motions associated with cooling at cloud top and warming at cloud base, there is likely to be a significant increase in concentrations and reduction in size of droplets and ice particles. Then the Twomey (1977) effect of increases in cloud opacity could produce increases in optical depth and downward irradiance at high latitudes as observed.

An indication of the strength of the repulsive forces involved in electro-anti-scavenging can obtained by comparing on the one hand the electric potential of charged particle approaching a charged droplet, and on the other hand the thermal kinetic energy of the particle in the line of centers. For q = 1e ($1.6\text{x}10^{-19}$C) on the particle and Q = 50e on a droplet of R = 3 μm radius, and at a temperature of T= 263K we have $Qq/(4\pi\varepsilon_0 R) = 3.75\text{x}10^{-21}$ Joules. This can be compared with the average energy of the distribution of the particle velocities in the line of centers; ½kT = $1.8\text{x}10^{-21}$ J, where k is Boltzmann's constant. So collision is inhibited between these same-sign droplets and particles. The comprehensive Monte Carlo simulations, most recently by Zhang et al., (2018, 2019), confirm this.

So far the modeling of electro-anti-scavenging covers only two-body interactions. Electro-anti-scavenging for distributions of size and distributions of charge of droplets, ice crystals, and condensation and ice nuclei, and the effects on cloud development, have yet to be modeled. There is a need to first model size and electric charge distributions for the mixed particle types, and then to apply parameterized two-body electro-anti-scavenging to the distributions. So the plausibility of the linkages represented by the flow chart has yet to be supported by quantitative modeling, although there is no reason to rule out a result that would give magnitudes and timescales consistent with the observations. The modeling of charge distributions among interacting ions, aerosols, droplets and ice crystals in the presence of vertical mixing processes in clouds, that must first be carried out before the modelling of scavenging of the distributions can take place, is itself challenging. A beginning for such modelling was made by Yair and Levin (1989).

It should be noted that the effects analyzed above are for only a fraction of the total ionosphere-earth current density, so the effects of the steady component on cloud microphysics may have been tuned out of cloud models. It will require much further data analysis and modeling to test the above scenarios.

4. Conclusions

Infrared radiances from clouds and from the surface at Alert, Canada, have been analyzed for variations related to time variations of solar wind magnetic field within solar rotation periods, and for the variation of this on seasonal timescales. A representation of polar ionospheric potential incorporating the effects of IMF B_Y, B_Z, and the solar wind speed, is used in the correlations, instead of just IMF B_Y. This work has shown that for periods in the northern hemisphere winter months with less solar insolation (October through April or March) and more snow cover and less convection, the correlation coefficients, relating cloud irradiance to ionospheric potential changes driven by the solar wind, markedly increase over the all-year correlations. There are increases in the correlation coefficients when the correlations are made during intervals when the solar wind exhibits 2-sectors per solar rotation, compared to when it exhibits 4-sector or irregular structures.-

The irradiance changes imply changes in optical thickness of the clouds. The correlations with changes in overhead ionospheric potential that drive vertical current density through clouds are consistent with an hypothesized mechanism involving cloud responses to the vertical current density. The mechanism is based on the changing amounts of electrical charges deposited on droplets, ice particles, condensation nuclei and ice nuclei that affect their mutual collision and loss rates. The findings that the irradiance changes lag the ionospheric potential changes by 3-4 days, and also that the correlation coefficients increase when the longer duration 2-sector changes in the inputs are present, are consistent with time constants of days for the occurrence of macroscopic effects of changes in microphysical scavenging processes in clouds.

The electro-anti-scavenging process has been extensively modeled for two-body collisions, but there is a need to model electric charge distributions for mixed particle types in mixed size distributions, and then to apply parameterized electro-anti-scavenging processes to the distributions, in order to model changes in cloud development for comparison with the observations.

Acknowledgements and Data Availability Statement: We thank Dr. D. Weimer for helping us to access output from his model, and with Drs. W. R. Coley and R. A. Heelis for useful discussions. Dr. Tinsley is a professor emeritus and is self-funded. This work was funded in part by the Strategic Priority Research Program of CAS (Grant No. XBD 41000000) and the National Science Foundation of China (41971020, 41905059). The solar wind data is from https://omniweb.gsfc.nasa.gov/form/dx1.html.
The Weimer model can be accessed at: https://ccmc.gsfc.nasa.gov/requests/instant_run.php
The Alert irradiance data is from: https://www.esrl.noaa.gov/gmd/dv/data/index.php?category=Radiation&parameter_name=Surface%2BRadiation.

APPENDIX A

Solar wind 2, 4, and irregular/multiple sector structures 1973-2018

2-sector	4-sector	Irregular/multiple sector
1973 Dec 5 – 1975 Oct 17		1975 Oct 18 – 1976 Sept 26
1976 Sept 27 – 1977 July 19		1977 July 20 – 1977 Dec 6
	1977 Dec 7 – 1978 July 4	
1978 July 5 – 1979 Aug 28		1979 Aug 29 – 1980 June 28
	1980 June 29 – 1980 Dec 14	
1980 Dec 15 – 1981 July 19	1981 July 20 – 1982 Jan 12	
1982 Jan 13 – 1982 Dec 6		1982 Dec 7 – 1983 Jan 20
	1983 Jan 21 – 1984 Feb 29	
1984 Mar 1 – 1984 Nov 15	1984 Nov 16 – 1985 Apr 20	
1985 Apr 21 – 1985 Dec 8		1985 Dec 9 – 1987 Apr 30
	1987 May 1 – 1988 Oct 10	
1988 Oct 11 – 1989 May 25	1989 May 26 – 1990 June 1	1990 June 2 – 1993 Oct 26
1993 Oct 27 – 1994 Dec 6	1994 Dec 7 – 1995 June 24	1995 June 25 – 1996 Apr 19
	1996 Apr 20 – 1997 Mar 21	1997 Mar 22 – 1998 Mar 16
	1998 Mar 17 – 1998 Nov 30	
1998 Dec 1 – 1999 May 5	1999 May 6 – 2000 Jan 26	
2000 Jan 27 – 2000 July 13	2000 July 14 – 2001 Mar 25	

2001 Mar 26 – 2001 Sept 21		2001 Sept 22 – 2001 Oct 26
2001 Oct 27 – 2004 July 19	2004 July 20 – 2007 Aug 14	
2007 Aug 15 – 2008 Dec 17		2008 Dec 18 – 2010 Jan 10
2010 Jan 11 – 2010 Apr 12	2010 Apr 13 – 2011 Feb 28	
2011 Mar 1 – 2011 Dec 17	2011 Dec 18 – 2012 Sept 7	2012 Sept 8 – 2013 Feb 12
2013 Feb 13 – 2013 June 23	2013 June 24 – 2014 Oct 17	
2014 Oct 18 – 2015 Feb 22		2015 Feb 23 – 2015 June 7
2015 June 8 – 2016 Jan 17	2016 Jan 18 – 2016 Apr 1	
2016 Apr 2 – 2017 Mar 31		2017 Apr 1 – 2017 Oct 27
2017 Oct 28 – 2018 June 29		2018 June 30 – 2018 Nov 3

APPENDIX B. The effects of IMF B_Z and solar wind speed (Vsw), as well as IMF B_Y, on ionospheric potentials at high magnetic latitudes: a parameterization of the Weimer (1995, 1996) model.

B1. Introduction

Figure B1 shows plots of northern hemisphere solar wind-induced high magnetic latitude ionospheric potentials from the satellite-based empirical models Weimer (1995, 1996), as functions of magnetic latitude and magnetic local time, for four sets of values of IMF B_Y and B_Z. They all have the same solar wind magnetic field transverse to the Earth-Sun line, $B_T = \sqrt{(B_Y^2 + B_Z^2)} = 5$nT, and the same solar wind speed, Vsw = 450 kms^{-1}). These solar wind - induced potential for these cases range from +20 kV to -47 kV and are measured as offsets from the global ionospheric potential (relative to the Earth's surface) of about 250 kV generated by thunderstorms and highly electrified shower clouds. The global component has its own diurnal and seasonal and day-to-day variations due to variations in convective storm output. In Fig B1(a) and B1(c) , which are for positive B_Y (+4.5 nT), the solar wind imposed potential close to the north magnetic pole (marked with a black dot) is negative. The potential near the pole changes to positive in Figs B1(b) and B1(d) with negative B_Y (-4.5 nT).

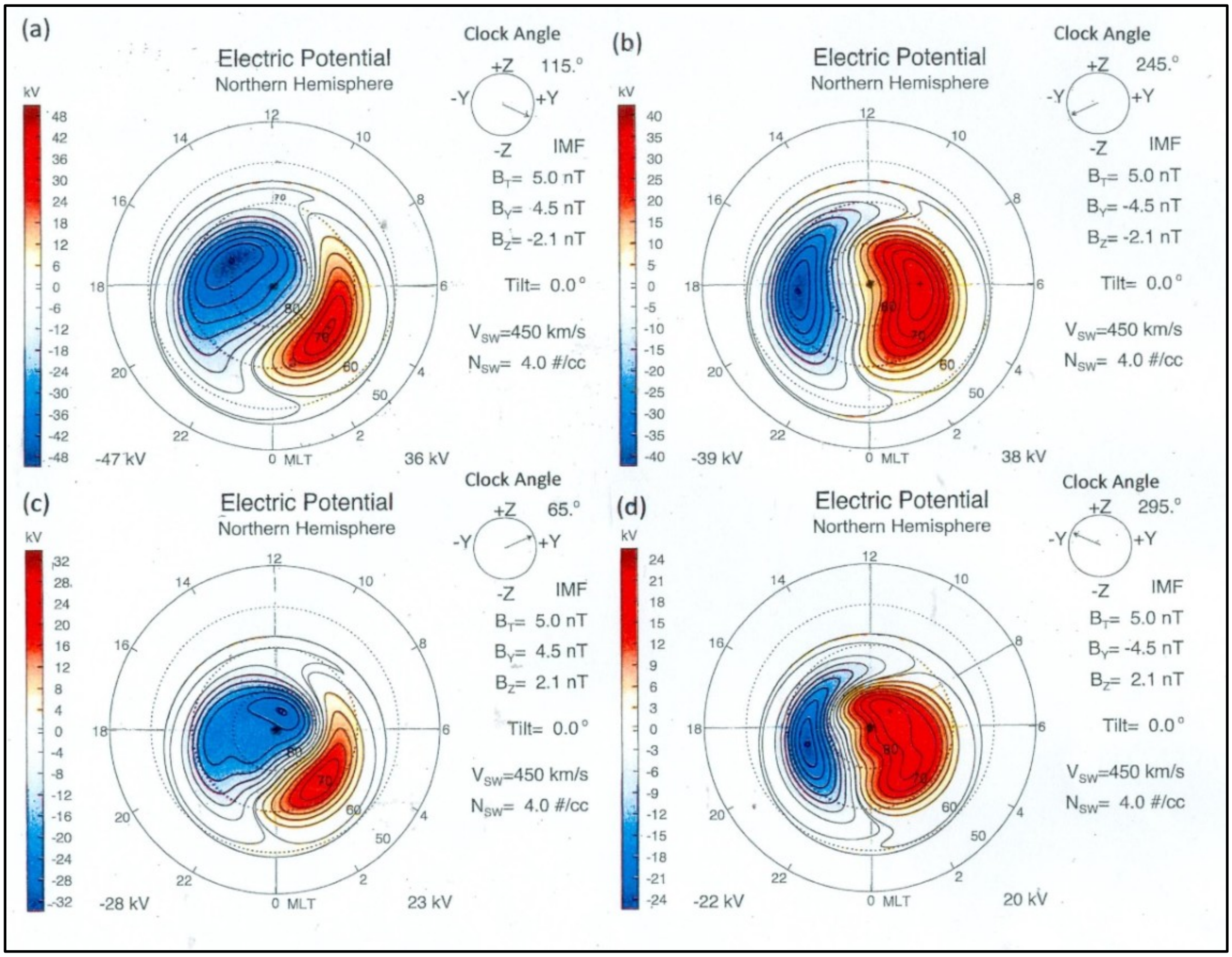

Figure B1. Solar wind–induced potential distributions over the northern high magnetic latitude regions as functions of magnetic latitude and magnetic local time. The data is from the empirical model of satellite observations by Weimer (1995, 1996). In each case the transverse IMF is 5 nT; the solar wind speed Vsw is 450 kms^{-1}; the plasma number density is 4 ions/cc., and the tilt of the Earth's dipole axis with respect to the plane perpendicular to the line to the sun is 0°. The four sets are for four different combinations of IMF B_y and IMF B_Z, with (a) and (c) for positive B_Y and (b) and (d) for negative B_Y. With (a) and (b) the B_Z component is negative, while for (c) and (d) it is positive, as indicated on the clock angle insert.

It is well known that the magnitudes of the dawn and dusk side convection cells depend on the B_Z component and also on Vsw. The sign of B_Z is negative in B1(a) and B1(b) and positive in B1(c) and B1(d). The magnitude of the overall potentials for both the dawn and dusk convection cells are greater in B1(a) and B1(b) with negative (southward) B_Z than for positive B_Z (northward), as noted on the panels. A similar dependence on B_Z and Vsw applies the potential at the magnetic poles, as will be subsequently demonstrated. So if it is in fact ionospheric potential that is responsible for the observed correlations of meteorological variables with B_Y, (Burns et al., 2008; Lam et al., 2013), then a representation of the potential that takes into account the effects of Vsw and B_Z could improve the correlations over just using B_Y alone. At a minimum, correlating with ionospheric potential rather than IMF B_Y transforms this study of sun-weather relations into one driven by changes in the global electric circuit in the atmosphere, rather than changes in the magnetic field in the solar wind, which is a different entity separated by ten earth radii from the surface weather.

It is important for inputs such as the downward current density, J_Z, which flows from the ionosphere to the surface through clouds, and is a candidate for effects on high latitude clouds, that the time scale for electrical effects on these stratus-type clouds to cause macroscopic changes is estimated to be the order of days. So, although the peak positive dawn (red in Fig B1) and negative dusk (blue in Fig B1) potentials are considerably higher than that at the pole, their effect on J_Z largely averages out as the Earth rotates, whereas the effect of B_Y on potential near the pole persists for up to 13 days for 2-sector solar wind structures, and 6 days for 4-sector structures.

So in this exercise we seek to parameterize the potentials at the north magnetic pole, VpN, using B_Z and Vsw as well as B_Y.

B2. Variations of ionospheric potential at the north magnetic pole.

The plots given in Fig 1 and the numerical values of potential corresponding to them can be accessed from the web site of the NASA/NSF sponsored Community Coordinated Modeling Center (CCMC), with its URL given in the Acknowledgements. As in Fig. B1, the data is available as a function of Vsw, B_Y and $B_{Z,}$ or as alternatives, B_T and the clock angle θ. This angle is defined by the signs and magnitudes of B_y and B_z in four quadrants, increasing clockwise (contrary to the analytical geometry convention of angle increasing anti-clockwise), as illustrated in Fig. B1. For B_Y +ve and B_Z +ve, $\theta = \tan^{-1}|B_Y/B_Z|$. For B_Y +ve and B_Z –ve, $\theta = 180^o - \tan^{-1}|B_Y/B_Z|$. For B_Y –ve and B_Z –ve, $\theta = 180^o + \tan^{-1}|B_Y/B_Z|$. For B_Y –ve and B_Z +ve, $\theta = 360^o - \tan^{-1}|B_Y/B_Z|$. The use of clock angle for ordering the potentials was found by Weimer to give a better empirical model than ordering by B_Z and B_Y separately. All the sets are for a fixed solar wind plasma density of 4 cm^{-3}, and tilt angle of the Earth's axis 0° with respect to the plane perpendicular to the Earth-Sun direction. For our purposes, working with correlations on the day-to-day timescale of daily averages, the tilt angle variation with season can be neglected, and values for 0° tilt (averages of satellite observations from -15° to +15° tilt angle) were used. Also, variations in plasma density (Nsw) were found to have a negligible effect on our parameterization, and the 4 cm^{-3} nominal value was used.

Figure B2 is a plot of the potentials at the north magnetic pole from the CCMC web site, for 21 clock angles for each of 9 combinations of Vsw and B_T, which are listed on the figure. At this web site, the clock angle convection is from -180° to +180°, corresponding to 0° to 360°. It is of interest that the potential in the model for zero B_T, at all clock angles and for Vsw from 300 to 800 km s^{-1}, is constant to within 0.6 kV of -12.9 kV, and that all the curves cross at clock angles of 36° and -174°. The peak potential in the range from -174° to 36° occurs at -77°, and the minimum in the range from 36° to 186° (= -174°) occurs at 112°. Although the maximum and minimum values are not midway between the crossing points, it is still not difficult to accurately parameterize these variations.

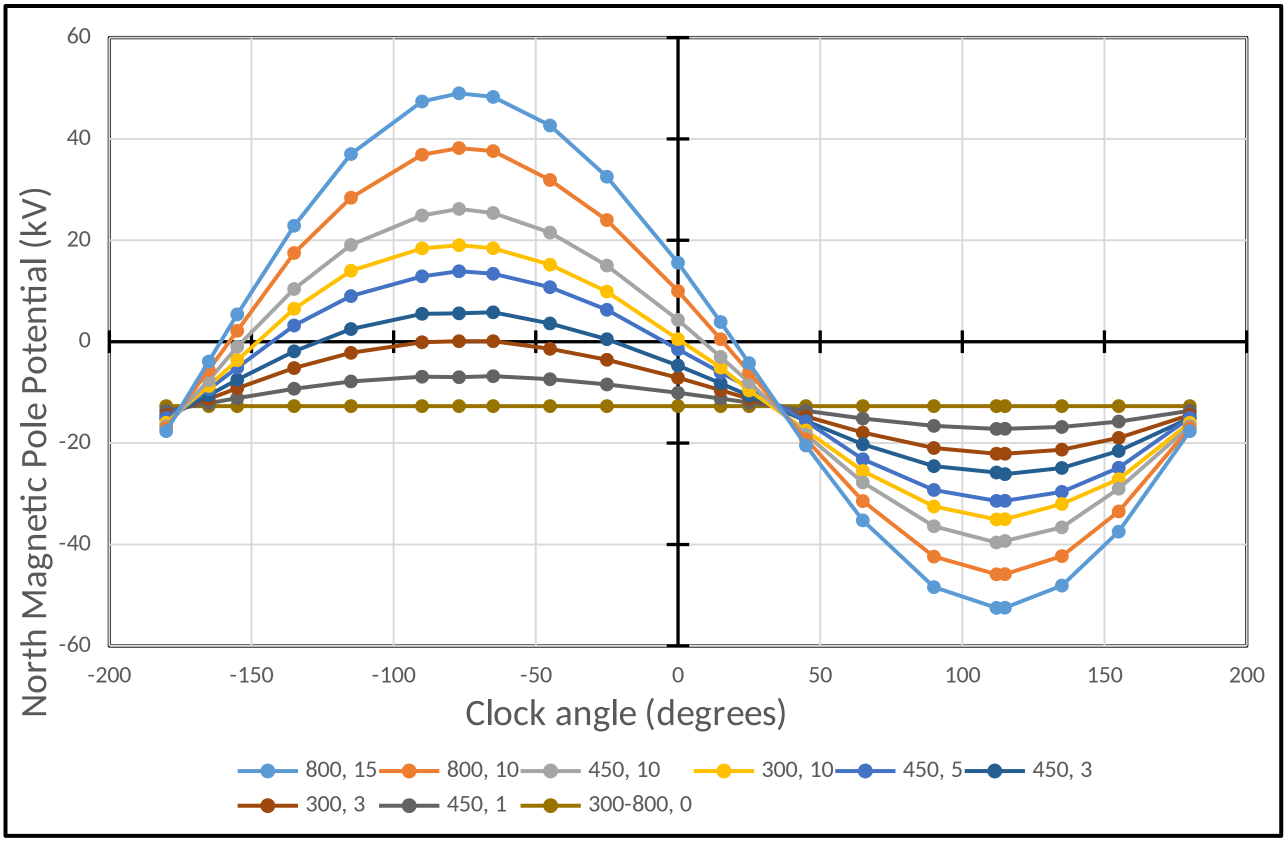

Figure B2. North magnetic pole potential (kV) as a function of clock angle from the Weimer model, for 9 sets of values of Vsw and B_T, and 21 clock angles, from -180° to +180°. The code for the colored dots is for Vsw, B_T.

The variations in polar potential with Vsw and clock angle (or B_Z)$_z$ are sufficiently large that we expect that taking them into account would change the correlations that have so far been found for surface pressure and cloud opacity only with B_Y, for stations near the north and south magnetic poles. The above potentials (VpN) apply to the north magnetic pole. For those for the south magnetic pole (VpS), the model applies with the sign of B_Y reversed, as noted by Weimer (1995). One interpretation of this reversal is that for ionospheric potential variations inside the auroral ovals the near-vertical magnetic field lines somehow connect to the solar wind and transmit electrical potentials generated by the solar wind Lorentz **V**x**B** electric fields to the Arctic and Antarctic ionospheres. Here **V** is the velocity of the Earth relative to the solar wind, directed towards the sun, and **B** is the interplanetary magnetic field (IMF), and the cross product gives an electric field perpendicular to both. The positive east-west, or B_Y, component of the IMF gives an electric field which is positive from south to north. Thus the ionospheric potential within about 15° of the south geomagnetic pole is increased, depending on B_Y, by 20 kV or so on average, while depressed near the north geomagnetic pole by about the same amount (e.g., Tinsley and Heelis, 1993, Lam et al., 2013). This interpretation accounts for the mostly positive potentials for negative B_Y and mostly negative potentials for positive B_Y near the pole in Fig. B2, and accounts for the opposite variation at the south magnetic pole, and for the potentials increasing in absolute magnitude with Vsw. However, it does not account for the effect of B_Z on the polar potentials. For just the Lorentz potentials the maxima and minima would be at clock angles of -90° and 90°. However the actual maxima and minima are shifted by 13° and 22° and occur at -77° and 112°.

The lobes of high potential on the dawn side and low potential on the dusk side of the auroral ovals are generated by solar-wind-induced field-aligned magnetospheric currents, which are strongly affected by the product of Vsw and B_Z component. While these must affect the potentials at the poles, it is not clear how this occurs. Nevertheless, the empirical sorting of the polar potentials into the dependency on B_T, Vsw and the clock angle in Fig. B2 suggests that an approximate expression for the near-polar potentials could be constructed, for use in making correlations with cloud properties and surface pressure at high latitudes in both polar regions.

Figure B3 is a plot of the potentials at the maxima (θ = -77°) and minima (θ = 112°) of the plots in Fig B2, extended to 21 different products of Vsw and B_T, using three different values of Vsw listed on the figure and color coded, and seven different values of B_T with each. It can be seen that the points for the different Vsw values form an overlapping trace within 1-2 kV, and this suggests a sufficiently accurate parameterization for the purpose of correlations with meteorological data would be to use as one variable the product of Vsw and B_T. The correlated signal in the meteorological data is a small fraction of the meteorological noise, whereas the errors in the fitting for ionospheric potential, without seeking very high accuracy in their representation, can be a small fraction of the signal. For the purpose of the correlations with meteorological data there is no point in seeking very high accuracy in parameterizing the potentials.

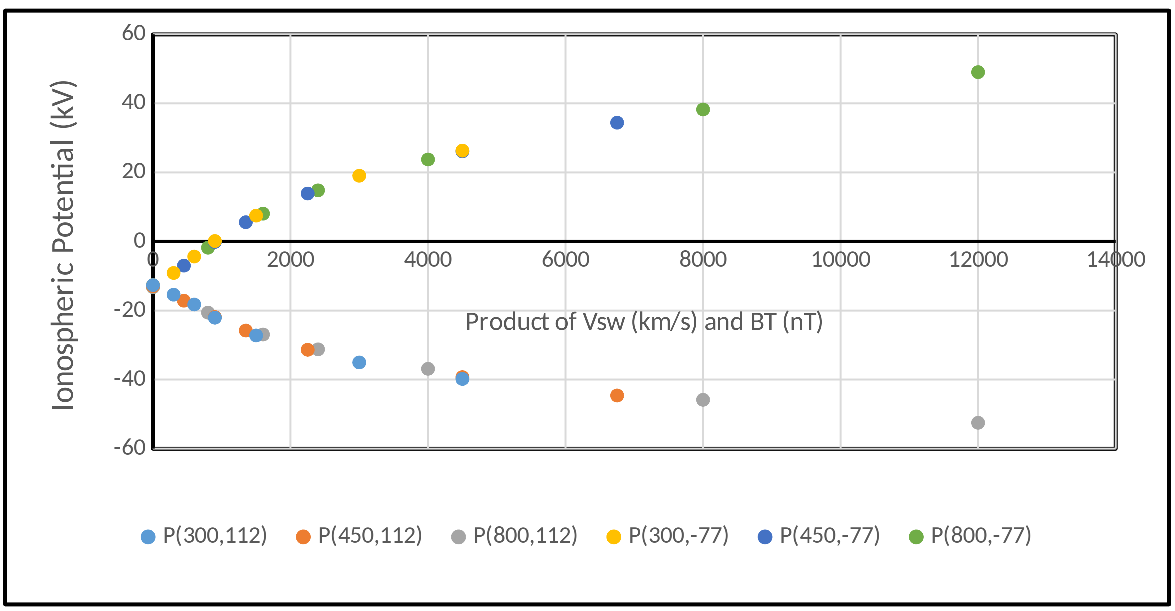

Figure B3. The maxima at clock angle θ = -77° and minima at clock angle θ = 112° of the variations of north magnetic pole potential, such as those in Fig B2, plotted against the product Vsw*B_T. The code for colored dots is (Vsw Clock angle).

Parameterization of the ionospheric potential at the north magnetic pole.

We define empirical fits to the curves of Fig. B2 in terms of expressions for potential, VpN in kilovolts, consisting of the product of an amplitude function, f(Vsw*B_T) for the difference of the maxima and minima from the zero BT level, as in Fig B3; a modified clock angle □ = g(θ) and its sine function; and the zero B_T level, i.e.

$$VpN = [f(Vsw^*B_T)^*\sin(g(\theta)) - 12.9 \text{ kV} \quad \ldots \ldots \quad \ldots \ldots \ldots. \text{(B1)}$$

This represents the variations of potential as in Fig B2. The modified clock angle is necessary in order that a simple sine function, ($\sin\phi$), can be used to represent the variations of potential with clock angle. Separate modified clock angle functions $\phi^+ = g(\theta+)$ and $\phi^- = g(\theta-)$ are needed, for the clock angle range from -174° to 36° and the range from 36° to 186° respectively. We require that the clock angle functions (ϕ) be zero at clock angles -174° (which is also 186°) and 36°, and also to be 90° at clock angles of -77° and 112°. Simple quadratic expressions are adequate for ϕ^+ and ϕ^-, and the result of fitting is

$$\phi^+ = 153.06° + 0.77081\theta - 6.256\times10^{-4}(\theta^2) \quad \ldots \ldots \quad \text{(B2)}$$

and

$$\phi^- = -41.77° + 1.15260\theta + 2.134\times10^{-4}(\theta^2) \quad \ldots \ldots \quad \text{(B3)}$$

For the function $f(Vsw^*B_T)$ two expressions, in these cases quartic polynomials, were similarly needed. These are $f^+(Vsw^*B_T)$ and $f^-(Vsw^*B_T)$. The result of the fitting is

$$f^+(Vsw^*B_T) = 1.6466\times10^{-2}(Vsw^*B_T) - 2.3649\times10^{-6}(Vsw^*B_T)^2 + 1.5613\times10^{-10}(Vsw^*B_T)^3 - 3.1298\times10^{-15}(Vsw^*B_T)^4 \quad \ldots \ldots \ldots \ldots \ldots \ldots \ldots \ldots. \quad \text{(B4)}$$

and

$$f^-(Vsw^*B_T) = -1.1848\times10^{-2}(Vsw^*B_T) + 1.9753\times10^{-6}(Vsw^*B_T)^2 - 1.71834\times10^{-10}(Vsw^*B_T)^3 + 5.5471\times10^{-15}(Vsw^*B_T)^4 \quad \ldots \ldots \ldots \ldots \ldots \ldots \ldots \ldots \quad \text{(B5)}$$

So for the clock angle range -174° < θ < 36° we have positive potential excursions above the negative $B_T = 0$ base, and

$$VpN = [(f^+(Vsw^*B_T)]\sin(\phi^+) - 12.9 \quad \ldots \ldots \ldots \quad \text{(B6)}$$

and for the clock angle range 36° < θ < 184° we have negative potential excursions below the negative $B_T = 0$ base, and

$$VpN = [(f^-(Vsw^*B_T)]\sin(\phi^-) - 12.9 \quad \ldots \ldots \ldots \quad \text{(B6)}$$

The standard deviation of the differences between the values of the above expressions and the Weimer model is less than 1.5 KV.

The two clock angle ranges are non-overlapping, so a single time series of VpN can be created by using values of clock angle (as daily averages, or on shorter time scales) to utilize one or other of the expressions in equations B5 or B6 to create the time series. In the Antarctic, the reversal of B_Y for evaluating the potentials changes the clock angle ranges. So to construct a time series VpS for southern high magnetic latitudes the clock angle range with positive potential excursions above the negative $B_T = 0$ base is from −36° < θ < 174°, and the range for the negative potential excursions below the negative $B_T = 0$ base is from 174° (−186°) < θ < −36°. There are corresponding changes required in ϕ^+ and ϕ^-.

References

Boberg, F., and H. Lundstedt, 2003. Solar wind electric field modulation of the NAO: A correlation analysis in the lower atmosphere. Geophys. Res. Lett., 30 (15) 1825, doi10.1029/2003GL017360

Burns, G. B., B. A. Tinsley, A. R. Klekociuk, O. A. Troshichev, A. V. Frank-Kamenetsky, M. J. Duldig, E. A. Bering, J. M. Clem, 2006. Antarctic polar plateau vertical electric field variations across heliocentric current sheet crossings, J. Atmos. Solar-Terr. Phys., 68, 639-654. Doi:10.1016/j.jastp.2005.10.008.

Burns, G. B., Tinsley, B. A., French, W. J. R., Frank-Kamenetsky, A. V., Bering, E. A. 2007. Interplanetary magnetic field and atmospheric electric circuit influences on ground-level pressure at Vostok. J. Geophys. Res. 112, D04103, https:// doi.org/10.1029/2006JD007246.

Burns, G. B., Tinsley, B. A., French, W. J. R., Troshichev, O. A., Frank-Kamenetsky, A. V., 2008. Atmospheric circuit influences on ground-level pressure in the Antarctic and Arctic. J. Geophys. Res. 113, D15112, https:// doi.org/ 10.1029/2007JD009618

Di Renzo, M., Johnson, P. L., Bassenne, M., Villafañe, L., Urzay, J., 2019. Mitigation of turbophoresis in particle-laden turbulent channel flows by using incident electric fields. Phys. Rev. Fluids, 4, 12430.

Frederick, J. E., 2016. Solar irradiance observed at Summit, Greenland: possible links to magnetic activity on short timescales. J. Atmos. Solar-Terr. Phys., 147, 59-70. https://doi.org/10.1016/j.jastp.2016.07.001

Frederick, J. E., 2017. An analysis of couplings between solar activity and atmospheric opacity at the South Pole. J. Atmos. Solar-Terr. Phys., 164, 97-104. https://doi.org/10.1016/j.jastp.2017.08.011

Frederick, J. E., Tinsley, B. A., 2018. The response of longwave radiation at the South Pole to electrical and magnetic variations: Links to meteorological generators and the solar wind. J. Atmos. Sol. Terr. Phys. 179, 214-224. https://doi.org/10.1016/j/jastp.2018.08.003.

Frederick, J. E., Tinsley, B. A., and Zhou, L., 2019. Relationships between the solar wind magnetic field and ground-level longwave irradiance at high northern latitudes. J. Atmos. Sol. Terr. Phys. 193,105063. doi:.org/10.1016/j.jastp.2019.105063.

Hays. P. B., and Roble, R. G., 1979, A quasi-static model of global atmospheric electricity; 1. The lower atmosphere. J. Geophys. Res., 84, 3291 -3305.

Humphries, R. S., Klekociuk, A. R., Schofield, R., Keywood, M., Ward, J., Wilson, S. R., 2016. Unexpectedly high ultrafine aerosol concentrations above East Antarctic sea ice. Atmos. Chem. Phys. 16, 2185–2206. http://dx.doi.org/10.5194/acp-16-2185-2016.

Khain, A., Arkhipov, V., Pinsky, M., Feldman, Y., Ryabov, Ya., 2004. Rain enhancement and fog elimination by seeding with charged droplets.Part 1 Theory and numerical simulations. J. Applied Meteorol. 43, 1513-1529.

Kniveton, D. R., Tinsley, B. A., Burns, G. B., Bering, E. A., Troshichev, O. A., 2008. Variations in global cloud cover and the fair-weather vertical electric field. J. Atmos. Solar-Terr. Phys., 70, 1633-1642, doi:10.1016/j.jastp.2008.07.001.

Lam, M. M., and B. A. Tinsley, 2016. Solar wind – atmospheric electricity – cloud microphysics connections to weather and climate, J. Atmos. Solar-Terr. Phys., 149, 277-290. doi.org/10.1016/j.jastp.2015.10.01.

Lam, M. M., Chisham, G., Freeman, M. P., 2013. The interplanetary magnetic field influences mid-latitude surface atmospheric pressure. Environ. Res. Lett. 8, 045001. https://doi.org/10.1088/1748-9326/8/4/045001.

Lam, M. M., Chisham, G., Freeman, M. P., 2014. Solar wind-driven geopotential height anomalies originate in the Antarctic lower troposphere. Geophys. Res. Lett. 41, 6509-6514. doi:10.1002/2014GL061421.

Lam, M. M., Freeman, M. P., Chisham, G., 2017. IMF driven change in the Antarctic tropospheric temperature due to global atmospheric electric circuit. J. Atmos. Solar-Terr. Phys., 180, 148-152, http://doi.org/10.1016/j.jastp.2017.08.027.

Lu, J. and Shaw. R.A., 2015. Charged particle dynamics in turbulence: theory and direct numerical simulations. Phys. Fluids., 27, 065111.

Mansurov, S. M., Mansurova, L. G., Mansurov, G. S., Mikhenvich, V. V., Visotsky, A. M. 1974. North-south asymmetry of geomagnetic and tropospheric events, J. Atmos. Solar-Terr. Phys., 36, 957-962.

Mareev, E. A., 2008. Formation of charge layers in the planetary atmospheres, Space Sci. Rev, 137. 373-393.

Markson, R. 1983. Solar modulation of fair-weather and thunderstorm electrification and a proposed program to test an atmospheric electrical sun-weather relationship, p.323-343 in "Weather and Climate Responses to Solar Variations", Colorado Associated University Press, Boulder Co. 626 pp.

Mauritsen, T., Sedlar, J., Tjernström, M., Leck, C., Martin, M., Shupe, M., Sjogren, S., Sierau, B., Persson, P. O. G., Brooks, I. M., Swietlicki, E., 2011. An Arctic CCN-limited cloud-aerosol regime. Atmos. Chem. Phys. 11, 165-173. https://doi.org/10.5194/acp-11-165-2011.

NASA/Goddard Space Flight Center, 2018. Space Physics Data Facility OMNIWeb Internet database, available at https://omniweb.gsfc.nasa.gov/form/dx1.html

Ness, N. F., and Wilcox, J. M., 1965. Sector structure in the quiet interplanetary magnetic field, Science, 148, 1592-1594.

Nicoll, K. A., 2012. Measurements of atmospheric electricity aloft, Surv. Geophys., 33, 991-1057.

Nicoll, K. A., Harrison, R. G., 2016. Stratiform cloud electrification: Comparison of theory with multiple in-cloud measurements, Quart. J. Roy. Meteorol. Soc., 142 (700), 2679-2691. doi.org/10.1002/qj2858.

NOAA, Earth System Research Laboratory, 2018. Surface radiation database, available at https://www.esrl.noaa.gov/gmd/dv/data/index.php?category=Radiation&parameter_name=Surface%2BRadiation

Page, D. E., 1989. The interplanetary magnetic field and sea-level polar pressure, in Workshop on Mechanisms for Tropospheric Effects of solar Variability and the Quasi-Biennial Oscillation, ed. S. K. Avery and B. A. Tinsley, p. 227-234. Univ. of Colorado, Boulder.

Pruppacher, H. R., Klett, J. D., 1997. Microphysics of Clouds and Precipitation. 2nd Ed., Springer, London.

Ramanathan, V., Subilsar, B., Zhang, G. J., Conat, W., Cess., R. D., Kiehl, J. T., Grassi, H., Shi, L., 1995. Warm pool heat budget and shortwave cloud forcing: A missing physics? Science, 267, 499-503.

Roble, R. G., and Hays, P. B., 1979. A quasi-static model of global atmospheric electricity; 2. Electrical coupling between the upper and lower atmosphere, J. Geophys. Res. 84, 7247-7256.

Rycroft, M. J., Nicoll, K. A., Aplin, K. L., Harrison, R. G., 2012. Recent advances in global electric circuit coupling between the space environment and the troposphere. J. Atmos. Solar-Terr. Phys., 90-91, 198-211.

Tinsley, B. A., 2008. The global atmospheric electric circuit and its effects on cloud microphysics. Rep. Prog. Phys. 71, 066801. https://doi.org/10.1088/0034-4885/71/6/066801.

Tinsley, B. A., Heelis, R. A., 1993. Correlations of atmospheric dynamics with solar activity: evidence for a connection via the solar wind, atmospheric electricity, and cloud microphysics. J. Geophys. Res. 98, 10375-10384.

Tinsley, B. A., Rohrbaugh, R. P., Hei, M. 2001. Electroscavenging in clouds with broad droplet size distributions and weak electrification. Atmospheric Research, 59, 111-135.

Tripathi, S. N., Vishnoi, S., Kumar, S., Harrison, R. G., 2006. Computationally efficient expressions for the collision efficiency between electrically charged aerosol particles and cloud droplets, Quart. J. Roy. Meteorol. Soc., 132, 1717-1731.

Twomey, B., 1977.The influence of pollution on the shortwave albedo of clouds, J. Atmos. Sci., 34, 1149-1152.

Wang, P. K., 2002. Ice Microdynamics, Academic Press, San Diego, CA.

Weimer, D. R., 1995. Models of high-latitude electric potentials derived with a least error fit of spherical harmonic coefficients, J. Geophys. Res., 100, (A10), 19595-19607.

Weimer, D. R., 1996. A flexible, IMF dependent model of high latitude electric potentials having "space weather" applications. Geophys. Res. Lett., 23(18), 2549-2552.

Wilcox, 1. M., Scherrer, P. H., Svalgaard, L., Roberts, W.O., and Olson, R. H., 1973. Solar magnetic structure: relation to circulation of the Earth's atmosphere, Science, 180, 185-186, 1973.

Yair, Y., and Levin, Z, 1989. Charging of polydispersed aerosol particles by attachment of atmospheric ions. J. Geophys. Res., 94, D11, 13,085-13,091.

Zhang, L., and Tinsley, B. A., 2017. Parameterization of aerosol scavenging due to atmospheric ionization under varying relative humidity, J. Geophys. Res. Atmos., 122, 5330-5350. doi:10.1002/2016/JD026255.

Zhang, L., and Tinsley, B. A., 2018. Parameterization of aerosol scavenging due to atmospheric ionization: 2 Effects of varying particle density, J. Geophys. Res. Atmos., 123, 3099-3115. doi:10.1002/2017/JD027884.

Zhang, L., Tinsley, B. A., Zhou, L., 2018. Parameterization of in-cloud aerosol scavenging due to atmospheric ionization, Part 3. Effects of varying droplet radius. J. Geophys. Res. Atmos. 123, 10,546-10,567. https://doi.org/10.1029/2018JD028840.

Zhang, L., Tinsley, B.A., Zhou, L., 2019. Parameterization of in-cloud aerosol scavenging due to atmospheric ionization, Part 4. Effects of varying altitude. J. Geophys. Res. Atmos. 124, 13,105-13126. https://doi.org/10.1029/2018JD030126.

Zhou, L., Tinsley, B.A., 2007. Production of space charge at the boundaries of layer clouds. J. Geophys. Atmos. 112, D11203, doi:10.1029/2006JD007998. https://doi.org/10.1029/2006JD007998.

Zhou, L, and Tinsley, B. A., 2012. Time dependent charging of layer clouds in the global electric circuit. Adv. Space Res., 50, 828-842. Doi:10.1016/j.asr.2011.12018.

Zhou, L., Tinsley, B. A., Wang, L., Burns, G., 2018. The zonal-mean and regional tropospheric pressure responses to changes in ionospheric potential. J. Atmos. Solar-Terr. Phys., 171, 111-118, http://dx.doi.org/10.1016/j.jastp.2017.07.010.

Captions for figures

Figure 1. Time series of IMF By (top panel), IMF B_z (middle panel) and solar wind speed (lower panel) July 2005 to June 2009, from NASA (2018). Intervals of sector structure are designated 2-sector, 4-sector or variable (irregular or more than 4 sectors). The 2-sector structure begins in July 2007.

Figure 2. Diagrams of East-West sections through the northern hemisphere of the global electric circuit, top: from Markson, (1983) showing the dawn and dusk ionospheric potential changes induced by IMF B_Z, and bottom; from Tinsley and Heelis, (1993) the potential changes induced by IMF B_y.

Figure. 3. Correlation in a running 27-day interval between the daily mean downwelling infrared irradiance (D_IR) and the upwelling irradiance (U_IR) measured at Alert, Canada 2004-2015. Data for June-July 2007 and small intervals in 2013-2014 are missing.

Figure 4. Lagged correlations for all seasons and all sector types of D_IR and U_IR with ($-B_y$), blue and orange curves respectively; and with VpN, green and red curves respectively, 2004-2015.

Figure 5. Lagged correlations for each October through April and all sector types of D_IR and U_IR with ($-B_y$), blue and orange curves respectively; and with VpN, green and red curves respectively, 2004-2015.

Figure 6. Lagged correlations with VpN for each October through April of D_IR (blue) and U_IR (red); also for each June-August with D_IR (grey) and U_IR (yellow); for combined 2 & 4 sector solar wind intervals, 2004-2015.

Figure 7. Lagged correlations of 2-sector U_IR values with VpN for October-April intervals: Oct 1 2007 to Nov 17 2008 (orange); Jan 11 2010 to Feb 22 2015 (blue): Overall correlation, (black).

Figure 8. Lagged correlation with VpN for isolated -7d to +7d portions of + to - SBCs of Alert irradiance data, 2004-2015. For October-March intervals for all sectors, D_IR (grey) and U_IR (yellow); and for just 2-sectors, D_IR (orange) and U_IR (green). There were 52 SBCs all-sector and of them 19 two-sector SBCs in this analyses.

Figure 9. Lagged correlation with VpN for isolated -7d to +7d portions of – to + sectors of Alert irradiance data, 2004-2015. For October-March intervals for all sectors, D_IR (grey) and U_IR (yellow); and for just 2-sectors, D_IR (orange) and U_IR (green). There were 47 SBC all-sector and of them 17 two-sector SBCs in this analysis.

Figure 10. Smoothed superposed epoch analyses of changes in Alert irradiances and VpN across + to - sector boundaries, for all-sector D_IR (blue) and U_IR (green) and 2 sector D_IR (yellow) and U_IR (orange). The irradiance changes can be compared to changes in VpN/3 (red). Data for each October through March, 2004-2014. The units of irradiance are W/m^2. Six units of VpN/3 correspond to 18 kV of the ionospheric potential change. There were 52 all-sector SBCs and of them 19 two-sector SBCs in this analysis.

Figure 11. Smoothed superposed epoch analyses of changes in Alert irradiance and VpN across – to + sector boundaries, for all-sector D_IR (grey) and U_IR (yellow) and 2-sector D_IR (orange) and U_IR (green). The irradiance changes can be compared to VpN/3 (red). Data for October - March, 2004-2015. The units of irradiance are W/m^2. Six units of VpN/3 correspond to 18 kV of the ionospheric potential change. There were 47 all-sector SBCs and of them 14 two-sector SBCs in this analysis.

Figure 12. Flow chart of inputs and links influencing atmospheric electric interactions with clouds. Links involving deposition of electric charge on droplets and aerosol particles, influencing the microphysical electro-scavenging and electro-anti-scavenging processes in clouds, are shown in heavier lines.

Figure B1. Solar wind–induced potential distributions over the northern high magnetic latitude regions as functions of magnetic latitude and magnetic local time. The data is from the empirical model of satellite observations by Weimer (1995, 1996). In each case the transverse IMF is 5 nT; the solar wind speed Vsw is 450 kms^{-1}; the plasma number density is 4 ions/cc., and the tilt of the Earth’s dipole axis with respect to the plane perpendicular to the line to the sun is 0°. The four sets are for four different combinations of IMF B_Y and IMF B_Z, with (a) and (c) for positive B_Y and (b) and (d) for negative B_Y. With (a) and (b) the B_Z component is negative, while for (c) and (d) it is positive, as indicated on the clock angle insert.

Figure B2. North magnetic pole potential (kV) as a function of clock angle from the Weimer model, for 9 sets of values of Vsw and B_T, and 21 clock angles, from -180° to +180°. The code for the colored dots is for Vsw,B_T.

Figure B3. The maxima at clock angle θ = -77° and minima at clock angle θ = 112° of the variations of north magnetic pole potential, such as those in Fig B2, plotted against the product Vsw*B_T. The code for the colored dots is (Vsw Clock Angle).